LATVIAN JOURNAL of PHYSICS and TECHNICAL SCIENCES

1

(Vol. 58)

2021

CONTENTS

Language Editor: O. Ivanova
Computer Designer: I. Begicevs

THERMOLUMINESCENCE RESPONSE OF AlN+Y$_2$O$_3$ CERAMICS TO SUNLIGHT AND X-RAY IRRADIATION

J. Cipa*, L. Trinkler, B. Berzina

Institute of Solid State Physics, University of Latvia,
8 Kengaraga Str., Riga, LV-1063, LATVIA
*e-mail: janis.cipa@cfi.lu.lv

AlN is a wide band gap material with promising properties for dosimetric applications, especially in UV dosimetry. In the present research, the thermoluminescence method is used in order to better understand sunlight and X-ray irradiation effects on yttria doped AlN ceramics. In general, the TL response is characterised by a broad TL peak with maxima around 400–450 K and a TL emission spectrum with UV (400 nm), Blue (480 nm) and Red (600 nm) bands. Compared to the X-ray irradiation, sunlight irradiation creates a wider TL glow curve peak with a maximum shifted to higher temperatures by 50 K.

Furthermore, in the TL emission spectra of AlN irradiated with sunlight the UV band is suppressed. The reasons of the TL peculiarities under two types of irradiation are discussed. Practical application of AlN ceramics as material for UV light TL dosimetry and, in particular, for sunlight dosimetry is estimated.

Keywords: *AlN, sunlight, thermally stimulated luminesce, UV light dosimetry, X-ray radiation.*

1. INTRODUCTION

Thermally and optically stimulated luminesce can be used to understand defect structure of materials, but in some cases the investigated material can have a combination of desirable dosimetric properties such as high response to irradiation, large linear dynamic dose range, stable signal during storage and others, making it suitable as a dosimetric material. AlN is one of such materials. There are currently commercially available dosimeters such as LiF:Mg,Cu,P (TL) Al$_2$O$_3$:C (OSL) and others, which can be used for different applications. Nevertheless, there is a demand for new dosimetric materials in some dosimetry areas, such as OSL neutron dosimetry, 2D dose

mapping, temperature sensing, UV dosimetry and others [1], [2].

UV light dosimetry is important because exposure to solar ultraviolet radiation is considered a risk to public health due to the increase of skin cancer incidence in the world; besides, the work environment with the use of UV light such as welding and water treatment cannot be monitored properly as there is not a lot of choice for dosimetric materials. Some thermoluminescence detectors have been studied as possible UV light dosimeters (LiF:Mg, CaF_2:Dy, CaF_2:Mn, Al_2O_3, LiF:Mg, $CaSO_4$:Dy, CaF_2:TB_4O_7, Vycor glass), but only few of them have found practical application: Al_2O_3:C (TLD-500) and $CaSO_4$:Dy (TLD-900) [3]. They show promising features but also have some certain disadvantages; thus, new dosimetric materials sensitive to UV light are required. In case of AlN, its spectral absorption is similar to that of human skin. Furthermore, it has a high TL response intensity and a large linear dose region. Thus, it might be a perspective UV dosimeter [4]. The main disadvantage of AlN is a high signal fading rate at room tempera-ture, which is not acceptable for dosimetric material. There are multiple ways how to solve this problem, one of them is thermal pre- or post-treatment [5].

To improve dosimetric properties of material, it is critical to understand TL mechanisms and defect structure, which has been thoroughly studied before [4], [6]. The previous studies [7] have shown that AlN ceramics reveals high sensitivity both to ionizing radiation and to UV light; however, each type of radiation provides its own characteristic features of the produced TL signal. In our previous study of luminescence processes induced by UV light irradiation, including TL, it was confirmed that both delocalised and localised electron transitions occur in AlN [8]. Here by delocalised electron transitions we understand those, which take place through the conduction band, while the localised transitions occur directly through tunnel recombination between donor and acceptor centres.

The main efforts of this study are focused on understanding the differences in TL response for AlN+Y_2O_3 irradiated with sunlight and X-rays.

2. EXPERIMENTAL

2.1. Sample Preparation

AlN+Y_2O_3 samples were produced at Riga Technical University by sintering ceramics from mixture of powders. AlN macro powder (20–80 μm, high purity, STREM Chemical Inc) was mixed with Y_2O_3 2 wt% (purity 99.9 %, Fluka) using Fritsh grinding apparatus for 30 min. Though the AlN raw material is nominally pure, it contains traces of Mn impurity revealed in photoluminescence (PL) and TL spectra as an emission band at 600 nm. A graphite press form with diameter of 20 mm was filled with the prepared powder mix-ture. The press form was placed in a spark plasma sintering apparatus and heated up to 1973 K for 10 min. The obtained AlN +Y_2O_3 ceramics samples with diameter of 20 mm and height of 2 mm were cleaned from admixture of graphite and cut into four pieces for further studies.

The phase composition and crystallite size were determined using an X-ray diffraction (XRD) analysis. Samples of sintered AlN with Y_2O_3 showed characteristic AlN diffraction patterns and contained traces of $Al_5Y_3O_{12}$ compounds. Crystallite

size of the samples was in the range of 56–67 nm depending on sintering temperature, holding time and composition.

2.2. Methods and Equipment

The TL measurements were done with Lexsyg Research TL/OSL reader from Freiberg Instruments. Two types of sample irradiation were used: natural sunlight and X-rays. Sample irradiation with sunlight occurred in summertime when the number of sunny days was the largest.

The Sun emission spectrum on the ground level is shown in Fig. 1 [9]. Its short wavelength part is limited by atmospheric absorption at around 290 nm. In the scope of this study, three types of optical glass filters were used. Their spectral transmission is shown in Fig. 1. Originally, filters are designated by Cyrillic letters; here in the text we give their Latin transcription.

Sample irradiation with X-rays was done by an X-ray source (W anode, anode voltage: 40 kV, anode current: 0.5 mA, irradiation time: up to 60 sec) integrated in the TL reader. To obtain spectra of TL, Andor SR-303i-B spectrometer with DV420A-BU2 CCD (150 lines/mm, 500 nm blaze) camera was coupled to Lexsyg TL/OSL reader with Ultra low-OH Molex optical fiber. While for TL glow curves the integrated Hamamatsu PMT R13456 with spectral range of 185–980 nm was used.

TL was measured at a heating rate of 1 K/s, up to maximum temperature of 700 K where the thermal radiation of the heater was limited by an infrared region and did not interfere with the TL signal. Previous studies have reported an intense afterglow signal for the irradiated AlN ceramics. Thus, after each irradiation a 10-minute delay time was used to decrease the influence of afterglow to < 1 %.

In order to clear up the optically stimulating effect of the visible range of the Sun emission on the stored TL response, the previously sunlight-irradiated $AlN+Y_2O_3$ sample was exposed to sunlight for 10 minutes through the ZHS16 optical filter, transmitting light with wavelengths longer than 450 nm (see Fig. 1). The obtained TL response was compared with that from the reference sample kept in darkness after irradiation. This method is further designated as sunlight optical stimulation (OS).

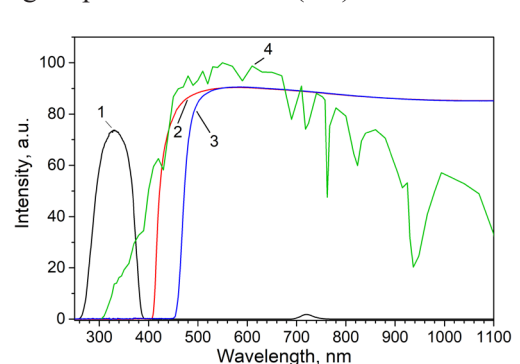*Fig. 1.* Transmission spectra of optical glass filters: 1) UFS2, 2) ZHS11, 3) ZHS16 used in this study and 4) the Sun emission spectra on the ground level (redrawn from [9]).

3. RESULTS

3.1. TL Characteristics after Irradiation with Sunlight

To determine the UV light-induced TL properties, we used the Sun as a natural UV light source. We used optical filters to select UV and visible spectral ranges of

the sunlight. It is known that UV light of the Sun emission spectra can excite TL in AlN+Y_2O_3, but also the visible light with wavelengths above 400 nm produces a weak TL signal. Temperature/wavelength contour plots of TL signal from AlN+Y_2O_3 ceramics irradiated with the sunlight without any filters and through UV and yellow filters are displayed in Fig. 2.
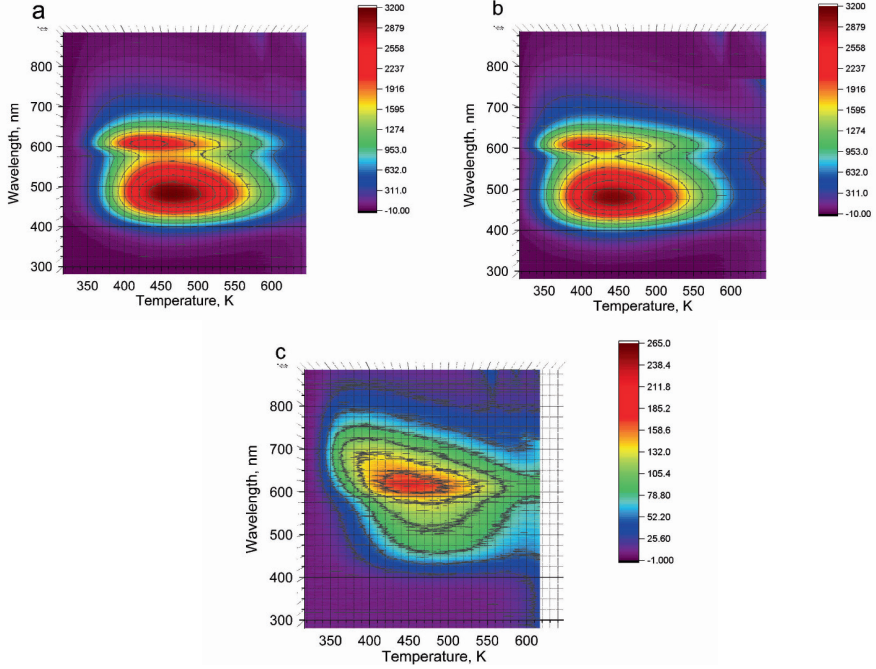
Fig. 2. Contour plots of AlN+Y_2O_3 ceramics irradiated with sunlight: a) without filters; b) through UFS2 filter and c) through ZHS11 filter.

3.1.1. TL Emission after Sunlight Irradiation

Let us compare TL emission spectra of AlN+Y_2O_3 and photoluminescence (PL) emission spectrum. According to the photoluminescence spectra described in our previous papers [10], PL spectrum contains several emission bands: a wide complex band at 400–550 nm, combined with 400 nm and 480 nm emission bands, associated with V_{Al}-O_N and V_{Al}-$2O_N$ centres, respectively, and 600 nm band attributed to Mn defects [4]. Hereafter, we denote these emission bands as UV, Blue and Red bands, accordingly. All these emission bands occur due to radiative recombination processes between donor and accepter centres.
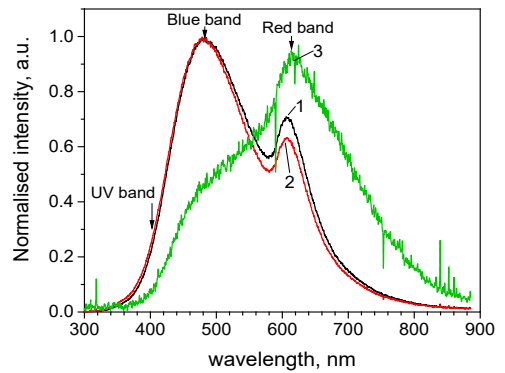
Fig. 3. Normalised TL emission spectra of AlN+Y_2O_3 at 460 K after irradiation with sunlight trough different optical filters: 1) no filter, 2) UFS2 and 3) ZHS11.

The TL emission spectrum contains the same UV, Blue and Red sub-bands as the PL emission spectrum. As seen in Fig. 3, their relative contribution depends on the optical glass filters used during irradiation with sunlight, i.e., on the wavelengths of the irradiation light. Under sunlight irradiation without filters (curve 1), the combined UV+Blue band is dominant over the Red band. Use of the UV filter UFS2 during sunlight irradiation causes a moderate decrease in the intensity of the Red band (curve 2), while ZHS11 filter reduces the total intensity of the TL signal, mainly at the expense of the UV band, so that the Red band becomes dominant (curve 3).

This difference of TL emission spectra under different irradiation conditions can be explained by excitation spectra of AlN individual emission bands [4] and taking into account the concept of the localised electron transitions. In detail, the process of localised electron transitions is described for the UV band of AlN produced by tunnel recombination between V_{Al}-O_N and O_N centres in [8]. As a result, irradiation of the sample with wavelengths, corresponding to absorption of a particular defect centre followed by its excitation and ionisation, causes the predominant appearance of its emission band in the PL and TL emission spectra. It means that excitation with UV light (particularly with sunlight) is selective.
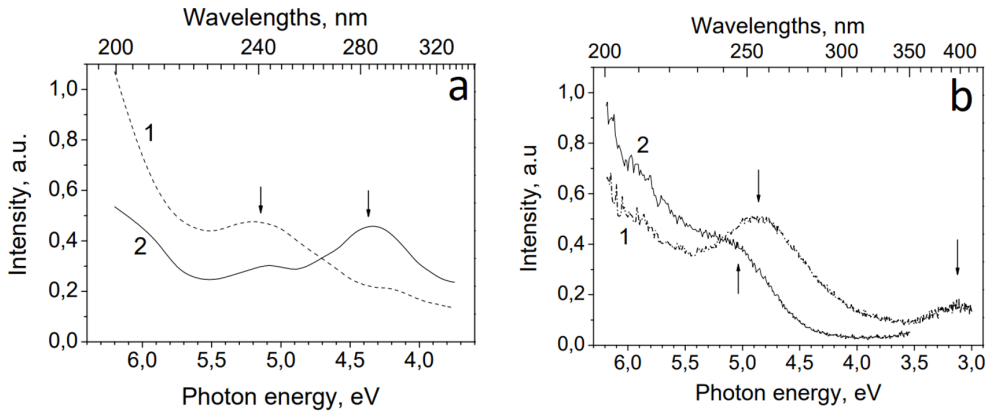
Fig 4. AlN ceramics excitation spectrum at 300 K: a) excitation spectra of 400 nm (1) and 480 nm (2) emission bands and b) excitation spectra of 600 nm band (1) and 400 nm band (2) [4].

Excitation spectrum of AlN ceramics covers a broad spectral range (see Fig. 4). The main excitation bands occur at 250 and 300 nm for the UV emission band, at 290 nm for the Blue emission band and at 260 and 410 nm for the Red emission band. Due to atmospheric absorption, sunlight wavelengths that are shorter than 290 nm do not reach the ground level and, therefore, do not participate in the excitation process. The UV filter UFS 2 cuts off the wavelengths above 390 nm, excluding the 410 nm band from the present excitation spectrum, thus causing reduction of the Red emission band, while still exciting the Blue band. The ZHS11 filter cuts off the wavelengths below 400 nm, eliminating the 290 and 300 nm bands, characteristic of the UV and Blue emission band excitation, from the excitation spectrum, and transmits the 410 nm band, thus decreasing the contribution of the UV (mostly) and Blue bands in favour of the Red band.

3.1.2. Analysis of TL Curves
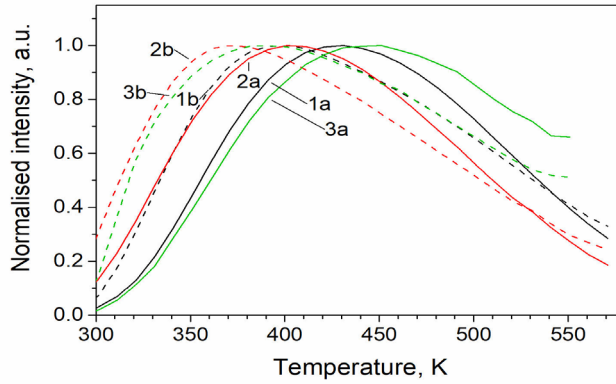
Fig. 5. TL curves after irradiation with sunlight through different optical filters:
1) no filter, 2) UFS2 and 3) ZHS11 for selected
(a) UV+Blue and (b) Red band emission.

Let us compare TL curves obtained after irradiation with sunlight from different spectral regions. Irradiation through the UV filter produces the TL curve peaking at 400 K, while sunlight irradiation without filter causes the TL curve peaking at 420 K. To explain this fact, it should be noted that the full sunlight spectrum causes both generation, predominantly in the UV spectral region, and destruction, in the visible region through the OS process, of the stored TL signal. When sunlight is used for irradiation without filters, both processes occur simultaneously. It is known [4] that the OSL process releases charge carriers from the shallow traps, which would contribute to the low temperature part of the TL curve. As a result, the TL curve obtained under irradiation with the full sunlight emission spectrum loses its low-temperature part and its maximum is shifted to higher temperatures.

Under similar irradiation conditions, the TL curves connected with the Red emission are shifted to lower temperatures compared with the UV+Blue emission (see corresponding curves in Fig. 5). It could be explained by the fact that Mn related trap centres are shallower than the intrinsic O and N related defects, which recombine at lower temperatures.

From our measurements, it is seen that maximum of the TL curves is located around 450 K (see Fig. 2). Yet there is an inconstancy with the results of our previous studies, where the TL curve maximum was found at around 600 K. Possible explanation might be in the different synthesis procedures of ceramic samples as well as different trace element concentration in raw materials. Similar results were reported in [11] where the authors used a synthesis method similar to ours, while slight changes in ceramics production procedure led to occurrence of the TL peak at temperature above 600 K [12], yet for both of these studies materials were obtained from the same material supplying company. Furthermore, even lower temperature maximum was observed in [13] where a different synthesis method was used. This fact indicates the importance of synthesis parameters such as time and temperature, as well as synthesis method and procedure.
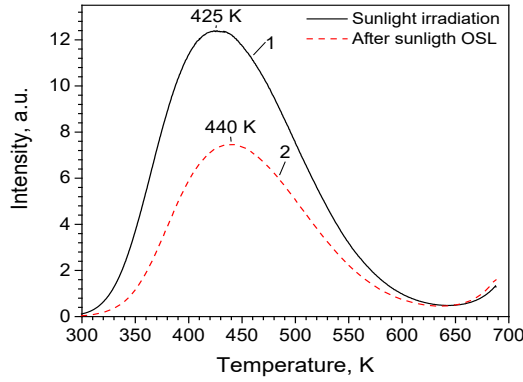
Fig. 6. TL glow curves 1) after irradiation sunlight for 10 min, and
2) after 10 min irradiation + 10 min sunlight OS (irradiation through ZHS16 filter).

As previously mentioned, sunlight both generates and depletes TL signal depending on the selected wavelengths. As for ZHS16 filter sunlight wavelengths shorter than 450 nm are cut off, the TL generating light is absent, but light from the remaining spectra depletes the trap centres. As it can be seen in Fig. 6, after irradiation through ZHS16 filter for the same time as irradiation time, only around half of TL intensity is left.

3.2. TL Characteristics after Irradiation with X-rays

Intensity of the Sun emission and its incident angle depends on a season, time of the day and weather conditions, making it problematic to repeat the accuracy of the experiment. Therefore, X-ray irradiation was chosen as a stable comparative irradiation type. Under X-ray irradiation electrons are transferred from the valence to the conduction band; relaxation of charge carriers is followed by generation of donor and accepter centres, charge carrier capture on luminescent ions and trapping centres. Mutual positioning of the generated luminescent centres and trapping centres is random. Thermal energy supply releases charge carriers from the trap centres; they participate in electron transitions (either delocalized – through the conduction band, or localized due to tunnelling) and radiative recombination. Due to random distribution of the recombination partners generated by the X-ray irradiation, occurrence of luminescence bands in X-ray induced TL emission is non-selective.
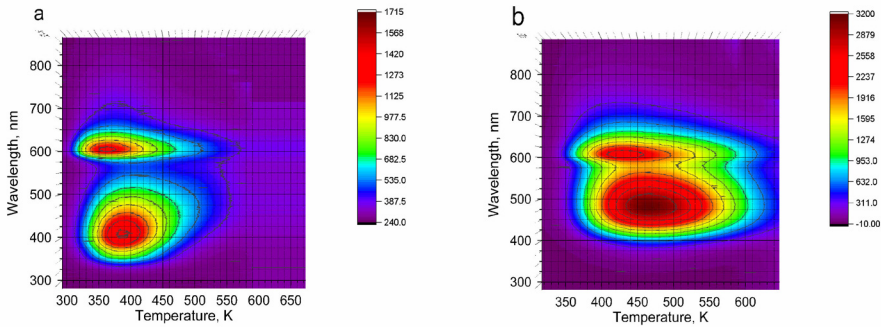
Fig. 7. TL contour plot for AlN + Y_2O_3 irradiated by X-rays for 20 sec
(a) and irradiated by sunlight for 10 min (b).

9
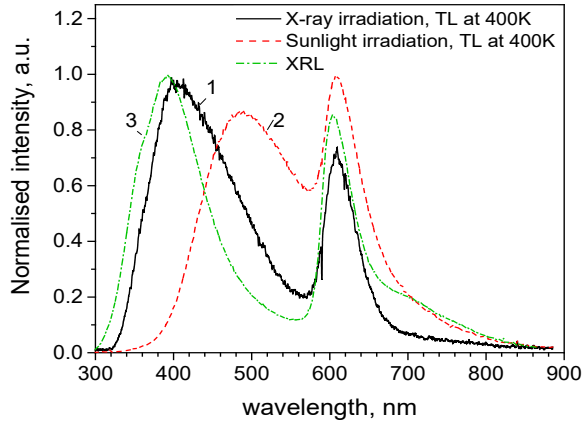
Fig. 8. Normalised TL emission spectra for AlN + Y_2O_3 irradiated 1) by X-rays for 20 sec and 2) by sunlight without filters for 10 min, and 3) X-ray luminescence. All spectra are measured at 400 K.
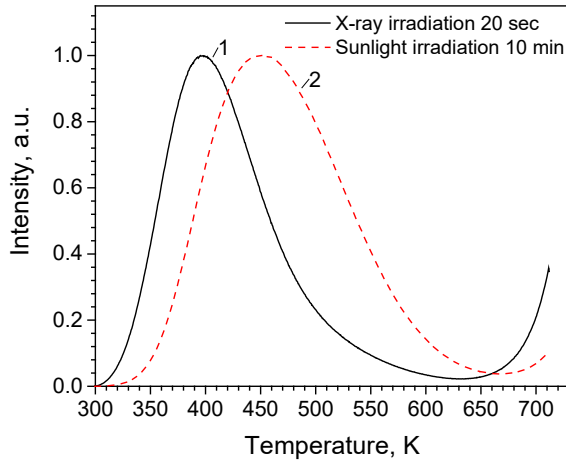
Fig. 9. AlN+Y_2O_3 TL glow curves after
1) X-ray and 2) sunlight irradiation for the integral spectrum.

Let us compare TL properties after irradiation with X-rays and with sunlight without optical filters. Figure 7 shows a noticeable difference between TL contour plots: there is a significant shift to higher temperatures and an essential change in the TL emission spectrum after irradiation with sunlight (Fig.7, b) compared to that with X-rays (Fig.7, a).

In case of AlN+Y_2O_3 ceramics samples the X-ray induced TL emission spectrum (Fig. 8, curve 1) is similar to X-ray luminescence spectrum (see Fig. 8, curve 3). Both spectra contain UV, Blue and Red bands. At the same time, it shows drastic dissimilarity from the sunlight-induced TL emission spectrum, which nearly has no UV band (Fig. 8, curve 2). The spectral difference can be attributed to the non-selective excitation of the UV+Blue bands by X-rays and their selective excitation by sunlight, keeping in mind the short wavelength limit of the sunlight on the ground level, preventing excitation of the UV emission band of AlN +Y_2O_3.

Comparison of the normalised TL

curves is shown in Fig. 9, where X-ray induced thermal curve is peaking at 400 K, while that after sunlight irradiation – at around 450 K. As already mentioned above, one reason for such a difference could be the optical destruction of the stored light sum by visible part of the sunlight spectrum.

Apart from the sunlight-induced OS process, another reason of the TL curve difference after different irradiation types might be related to unintentional heating of the sample during irradiation with sunlight.
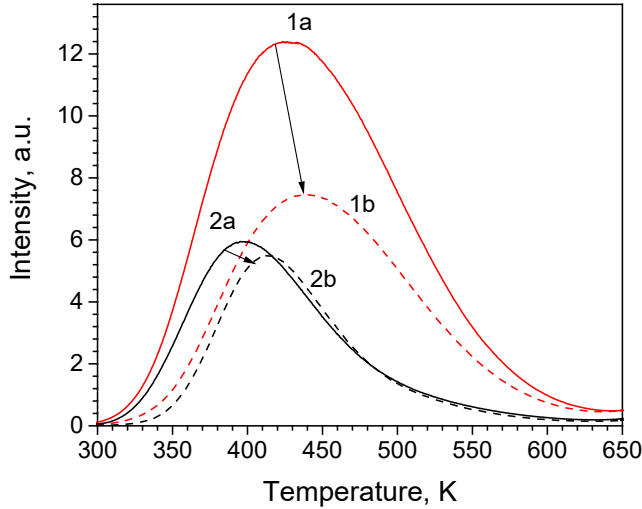
Fig. 10. TL glow curves after irradiation with no-filter sunlight for 10 min (1a) and after direct sunlight irradiation another 10 min irradiation through ZHS 16 filter (1b) and irradiation with X-rays for 20 sec (2a) and Xray irradiation and linear heating up to 330 K in 10 minutes (2b).

To estimate how the sunlight-induced OS and sample heating during irradiation affect the TL curve, a special experiment was implemented (see Fig. 10). It was estimated that during irradiation by sunlight $AlN+Y_2O_3$ sample might have been heated by approximately 30 K. Thus, further experiments with linear preheating up to 323 K after X-ray irradiation were implemented. The resulting TL curve is shown in Fig. 10, 2b. This TL curve is shifted by 20 K compared to the TL curve without pre-heating.

Secondly, the effect of sunlight OS was investigated. Figure 10 also shows that opti-cal stimulation with wavelengths above 450 nm in 10 minutes reduces TL signal by 40 % and shifts the peak maxima by 15 K. Analysing results of this experiment, it could be concluded that both OS and sample heating during sunlight irradiation reduce the stored TL signal.

In order to control the correctness of the TL response from $AlN+Y_2O_3$, it is recommended to keep the irradiated material in the darkness and to monitor temperature when samples are irradiated by sunlight.

4. POTENTIAL APPLICATION OF AlN IN UV DOSIMETRY

In this paper, we have investigated the main TL properties of $AlN+Y_2O_3$ after irra-diation with sunlight in comparison with that after X-ray irradiation in order to evalu-

ate its appropriateness as a UV light dosimetry material, and in particular as a material for the sunlight TL detection. In general, AlN ceramics shows rather high sensitivity to the natural sunlight, which is an advantage of the dosimetry material. However, spectral sensitivity of AlN is the highest in the range of 250–270 nm [14], while the Sun emission spectrum is limited by 290–300 nm at the ground level due to absorption by atmospheric oxygen, thus excluding the most favourable region of material sensitivity. Besides, using AlN ceramics for the sunlight dosimetry, one should take into consideration the optical stimulation effect from the light with wavelengths above 450 nm and possible heating of the sample during irradiation, both processes reducing the TL signal. To prevent these effects, optical filters are to be used.

Though AlN could be used for detection of the sunlight dose, its optimal application area lies in the spectral range of 200–300 nm. One of the application areas could be the antibacterial water treatment, where Hg lamps with characteristic emission line at 254 nm are used. This wavelength is particularly favourable for production of the TL signal in AlN ceramics, because it corresponds to the excitation of the UV emission band. AlN ceramics as a dosimetric material could be used to optimise bactericidal reactor configurations and water flow rate [15]. One more possibility could be space applications, where sunlight spectrum is not influenced by atmospheric absorption and AlN could serve as a good dosimeter for astronaut and equipment extravehicular activities [16].

The other effect preventing practical application of AlN for dosimetry is a high fading rate of the stored TL signal. We roughly evaluated a fading rate comparing TL glow curves just after irradiation and 24 h after irradiation. For AlN ceramics, it was determined that 24 h after irradiation the remaining intensity for X-ray irradiated samples was around 50 %, while for sunlight irradiation it was approximately 70%. Taking into account a high fading rate, AlN ceramics could be recommended for quick tests, where it would play an insignificant role.

5. CONCLUSIONS

To summarise, thermoluminescence in AlN+Y_2O_3 was investigated after irradiation with sunlight and X-rays. In general, the TL response is characterised with a broad TL peak with maxima around 400–450 K and TL emission spectrum with UV (400 nm), Blue (480 nm) and Red (600 nm) bands. However, there is a significant difference between TL characteristics obtained under irradiation with sunlight and X-rays.

It was found that after sunlight irradiation the obtained TL curve and TL emission spectrum depended on the optical filters used. Specific properties of the TL characteristics are explained by 1) the Sun emission spectrum at the ground level beginning at 290 nm; 2) simultaneous production of the TL signal (by $\lambda < 450$ nm) and its destruction (by $\lambda > 450$ nm) under sunlight irradiation; 3) selective character of production of defect recombination components depending on irradiation light wavelength correspondence to a particular defect absorption; 4) sample heating during irradiation sunlight. The proposed application areas of AlN ceramics as material for UV light TL dosimetry include water treatment and space industry, as well as public sector.

ACKNOWLEDGEMENTS

REFERENCES

1. Yukihara, E. G., Milliken, E. D., Oliveira, L. C., Orante-Barrón, V. R., Jacobsohn, L. G., & Blair, M. W. (2013). Systematic Development of New Thermoluminescence and Optically Stimulated Luminescence Materials. *Journal of Luminescence*, *133*, 203–210. https://doi.org/10.1016/j.jlumin.2011.12.018

2. Olko, P. (2010). Advantages and Disadvantages of Luminescence Dosimetry. *Radiation Measurements*, *45* (3–6), 506–511. https://doi.org/10.1016/j.radmeas.2010.01.016

3. Diffey, B. (2020). The Early Days of Personal Solar Ultraviolet Dosimetry. *Atmosphere*, *11* (2). https://doi.org/10.3390/atmos11020125

4. Trinkler, L., & Berzina, B. (2011). Luminescence Properties of AlN Ceramics and Its Potential Application for Solid State Dosimetry. *Advances in Ceramics – Characterization, Raw Materials, Processing, Properties, Degradation and Healing*. https://doi.org/10.5772/18658

5. Burgkhardt, B., Piesch, E., Physk, H., & Nuclear, K. (1978). The Effect of Post-Irradiation Annealing on the Fading Characteristic of Different Thermoluminescent Materials Part II – Optimal Treatment and Recommendations. *Nuclear Instruments and Methods*, *155*, 299–304. https://doi.org/10.1016/0029-554X(78)90219-7

6. Trinkler, L., Berzina, B., Kasjan, D., & Chen, L. C. (2007). Luminescence Properties of AlN Nanostructures Revealed under UV Light Irradiation. *Journal of Physics: Conference Series*, *93* (1). https://doi.org/10.1088/1742-6596/93/1/012040

7. Trinkler, L., Bøtter-Jensen, L., Christensen, P., & Berzina, B. (2001). Stimulated Luminescence of AlN Ceramics Induced by Ultraviolet Radiation. *Radiation Measurements*, *33* (5), 731–735. https://doi.org/10.1016/S1350-4487(01)00093-2

8. Trinkler, L., & Berzina, B. (2014). Localised Transitions in Luminescence of AlN Ceramics. *Radiation Measurements*, *71*, 232–236. https://doi.org/10.1016/j.radmeas.2014.02.016

9. Hulstrom, R., Bird, R., & Riordan, C. (1985). Spectral Solar Irradiance Data Sets for Selected Terrestrial Conditions. *Solar Cells*, *15* (4), 365–391. https://doi.org/10.1016/0379-6787(85)90052-3

10. Trinkler, L., Boøtter-Jensen, L., Berzina, B., Horowitz, Y. S., & Oster, L. (2002). Aluminium Nitrate Ceramics: A Potential UV Dosemeter Material. *Radiation Protection Dosimetry*, *100* (1–4), 313–316. https://doi.org/10.1093/oxfordjournals.rpd.a005876

11. Kojima, K., Okada, G., Fukuda, K., & Yanagida, T. (2016). Influence of SrF2-Doping in AlN Ceramics on Scintillation and Dosimeter Properties. *Radiation Measurements*, *94*, 78–82. https://doi.org/10.1016/j.radmeas.2016.09.008

12. Onoda, Y., Kimura, H., Kato, T., Fukuda, K., Kawaguchi, N., & Yanagida, T. (2019). Thermally Stimulated Luminescence Properties of Eu-Doped AlN Ceramic. *Optik*, *181* (November 2018), 50–56. https://doi.org/10.1016/j.ijleo.2018.11.160

13. Spiridonov, D. M., Weinstein, I. A., Chaikin, D. V., Vokhmintsev, A. S., Afonin, Y. D., & Chukin, A. V. (2019). Spectrally Resolved Thermoluminescence in Electron Irradiated AlN Submicrocrystals. *Radiation Measurements*, *122*, 91–96. https://doi.org/10.1016/j.radmeas.2019.02.001

14. Trinkler, L., & Berzina, B. (2001). Radiation Induced Recombination Processes in AlN Ceramics. *Journal of Physics Condensed Matter*, *13* (40), 8931–8938. https://doi.org/10.1088/0953-8984/13/40/307

15. Li, X., Cai, M., Wang, L., Niu, F., Yang, D., & Zhang, G. (2019). Evaluation Survey of Microbial Disinfection Methods in UV-LED Water Treatment Systems. *Science of the Total Environment, 659*, 1415–1427. https://doi.org/10.1016/j.scitotenv.2018.12.344

16. Dachev, T. P., Tomov, B. T., Matviichuk, Y. N., Dimitrov, P. G., & Bankov, N. G. (2016). High Dose Rates Obtained Outside ISS in June 2015 during SEP Event. *Life Sciences in Space Research, 9*, 84–92. https://doi.org/10.1016/j.lssr.2016.03.004

RE-EVALUATION OF CHROMIUM DOPED ALUMINA FOR DOSIMETRIC APPLICATIONS

E. Einbergs*, A. Zolotarjovs, I. Bite, J. Cipa, V. Vitola,
K. Laganovska, L. Trinkler

Institute of Solid State Physics, University of Latvia,
8 Kengaraga Str., Riga, LV-1063, LATVIA
*e-mail: ernestse@cfi.lu.lv

Many medical examinations involve ionizing radiation. Although the range of available dosimeters is rather wide, their linearity and chemical stability are limited. Recently, there has been a growing interest in new, improved dosimetric materials for emerging applications in medicine and other fields, such as sterilisation of consumer goods and medical instruments, irradiation of seeds, chemical agents and others.

One of the classical dosimeters is carbon-doped alumina (Al_2O_3:C) – a well-established and widely used material for personal and industrial dosimeter with a range of great properties, such as high sensitivity, wide linearity range and relative ease of production and handling. However, the demand for reliable dosimeters in a high-dose range is still only partially fulfilled, and alumina doped with chromium ions (Al_2O_3:Cr) can be a promising candidate.

In this study, we explored alumina doped with chromium porous microparticles synthesized with a sol-gel method as a possible high dose dosimeter and evaluated its thermostimulated luminescence signal, dose response with two irradiation sources and measured long-time fading. It was found that although the TSL signal was quite complex (consisting of two main peaks above room temperature) and the long-term fading was significant (around 50 % in the span of 30 days), with sufficient optimisation the material could be used as a high-dose dosimeter for X-ray and beta irradiation. Wide high dose linearity range, physical and chemical characteristics, as well as low production costs and ease of synthesis make chromium (III) doped alumina a compelling candidate for applicability in various medical and industry fields.

Keywords: *Alumina, chromium, dosimetry, sol-gel, Al_2O_3:Cr.*

1. INTRODUCTION

Ionizing radiation possesses a widespread applicability ranging from object identification during security checks to non-intrusive tumour passivation. However, irreversible impact on organic matter can occur with the extensive use of ionizing radiation, especially for extended periods of time. Scientific studies have proven that prolonged exposure (accumulation of irradiation) increases the risk of developing harmful tumours or other types of health issues [1]. To reduce the risks of degrading physical well-being of personnel involved in the usage or maintenance of irradiative equipment, the absorbed dose by the staff must be monitored and managed accordingly. Alongside the mentioned applications, dosimeters can be used in other applications, for example, as a means for determining the intensity of an ionizing radiation source or for discovering radiation leakage in order to thicken the shielding around a source.

Alumina-based dosimeters have been a point of interest for many research groups for some time due to a wide sensitivity range, high chemical stability and hardness, comparably low production costs and a stable signal at RT (room temperature). Multiple experiments were performed by Axelrod et al. with the goal of testing various dopants and expecting improved dosimetric properties, and it was discovered that carbon additives vastly improved thermostimulated luminescence (TSL) intensity, sensitivity, and linearity range. Carbon doped alumina (Al_2O_3:C), also known as TLD-500, is one of the best and widely used high sensitivity dosimeteric materials that possesses a wide linearity range (10 μGy – 10 Gy) [2]. Its main application as a TSL and OSL (optically stimulated luminescence) material is for medicine, such as radiotherapy, radiodiagnosis, and heavy charged particle dosimetry. However, due to the limitations of measurement setups at the time, chromium as an additive was discarded as the output signal was in the "red" region of the spectrum – outside of the peak sensitivity of photomultiplier tubes. Nevertheless, Al_2O_3:Cr was noted as a good candidate for OSL dosimetry. With recent advances in Si-based sensors, the "red" luminescence can be considered as an advantage; therefore, the Cr doping should be re-evaluated.

Recent technological advancements have created a demand for high dose dosimetric materials. Nanostructured chromium (III) oxide doped alumina has shown heigh sensitivity to gamma rays ranging from 100 Gy to 20 kGy without achieving saturation [3] and the luminescence during the pulse, and during the subsequent afterglow, are monitored as functions of time. The material under study is α-Al_2O_3:C. Data are presented on the dependence of the OSL intensity on: (i and in crystalline form up to 750 kGy [4]. Material could become ideal for applications involving high doses like irradiation of consumer goods, seeds, chemical agents and medical instruments.

The performance of most materials used for dosimetry applications is mainly governed by the impurity ions in the crystalline lattice coupled with lattice imperfections around them (with a meaningful difference in size or oxidation state compared to host ions). However, for practical applications of a particular material, the linearity range and fading must be explored. Most materials display a corelation between registered TSL or OSL signal and the dose of ionizing radiation they have been exposed to, but few exhibit a first degree (linear) corelation

in a wide enough region, also known as linearity range. Another factor that should be considered is fading, which largely contributes to host matrix properties and the depth of trap as the bulk of the lost signal can be attributed to phonon discharge, although some secondary effects can increase fading of relatively deep charge carrier traps.

In this article, we explore chromium (III) oxide doped alumina response to beta and X-ray radiation as well as fading over a period, which is typical of personal dosimeters.

2. EXPERIMENTAL

2.1. Materials

In the synthesis, analytical grade chemicals were used without further purification. Chromium (III) oxide (Cr_2O_3) and aluminium nitrate nonahydrate ($Al(NO_3)_3 \cdot 9H_2O$, purity 99.6 %, VWR Prolabo Chemicals) were used as starting materials. As chelating and polymerizable agents, ethylene glycol ($HO(CH_2)_2OH$, purity 99 %) and citric acid ($C_6H_8O_7$, purity 99.5 %) were used and purchased from Sigma Aldrich. Chromium (III) oxide was dissolved using nitric acid (HNO_3, assay 65 %) (Sigma Aldrich).

2.2 Chromium Doped and Undoped Alumina Synthesis

Undoped and chromium (III) doped alumina samples were synthesised with suspension and gelation (sol-gel) polymerized complex method, analogous to our previous publications [5]. Amount of added chromium (III) oxide ranged from 0 to 1.5 wt%. Mixtures were prepared at 1:1:4 molar ratio (metal ions to citric acid to ethylene glycol). Deionized water was added to create 0.2 molar solution. After obtaining the necessary consistencies, gels were heated in an open oven at 400 °C for 2 hours. Upon successful elimination of nitric oxide, black powder was formed, which was calcined for 4 hours at 1400 °C. Calcination yielded white powders with a faint pink shade.

2.3. Characterisation

The same samples as in our previous publication [6] were used, which consisted of a pure alpha phase and did not contain any major disruption in the crystalline lattice due to aforementioned chemical stability. Results gathered from EDX (energy-dispersive X-ray spectroscopy) were used to evaluate the presence of Cr atoms in the structure. SEM (scanning electron microscope) imaging provided information required to conclude that porous microceramics were created. XRL (X-ray luminescence), PL (photoluminescence) and TSL were used for evaluation of optical properties of the sample. Impurity or defect luminescence was below detection threshold. Luminescence intensity measurements proved to be inconclusive regarding determination of the optimal concentration of Cr_2O_3. The highest TSL readout intensity was registered for the sample with 0.2 wt%.

This study focuses on re-evaluation of Al_2O_3:Cr linearity range and fading over a month without the possibility of UV exposure. Measurements were conducted using Lexsygresearch LMS (Freiberg instruments) with X-ray and beta sources. Beta source (Sr90) provided a dose of 55 ± 5.5 mGy/s and samples were irradiated from 60 s to 8.3 h or from 3.3 Gy to 1.65 kGy. X-ray

measurements were made with 40 kV and 0.5 mA, tube consisted of a tungsten target, beryllium window and was powered by Spellman MNX50P50/XCC power supply. As multiple samples with slightly varying masses and surface area were prepared, calibration measurements were performed. Between measurements, samples were preheated to remove any previously accumulated dose, irradiated for 1200 s (with 66 Gy) and repeatedly measured. The highest registered intensity was taken as a baseline and an equalization coefficient was calculated for other samples, which was applied to avoid invalidation based on inconsistency.

SEM and EDS measurements were conducted using SEM Helious 5 UX (Thermo Fisher Scientific) operated at 2 kV during imaging and at 30 kV during an elemental analysis.

3. RESULTS

3.1. SEM and EDS Measurements

Results of SEM imaging are shown in Fig. 1. Samples consist of a dense ceramic-like structure with the slight porosity occurring through the grains. Multiple surface holes have been observed along grain boundaries. Grains appear to be polycrystalline with crystallite size of around 40 nm (calculated from the previously conducted XRD measurements using Scherrer equation).
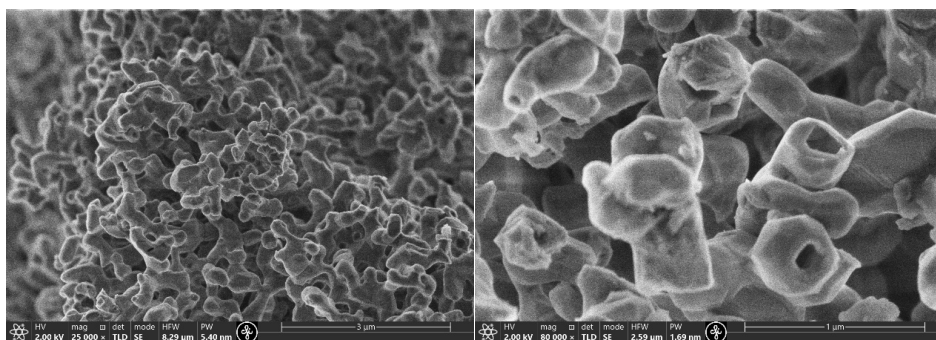
Fig. 1. SEM measurements with varying magnifications.

SEM EDX elemental analysis results are displayed in Fig. 2. The presence of Cr is confirmed by the corresponding peaks; however, the detection limit of the system forbids accurate evaluation of the absolute concentration value. Negligible amounts of silicon and calcium have been detected originating from different parts of sample synthesis and handling.
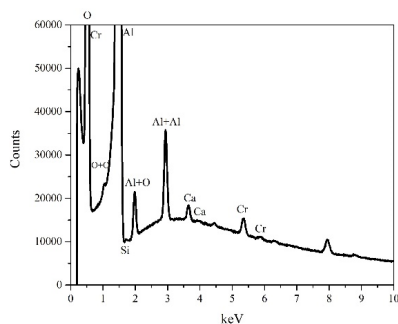
Fig. 2. SEM EDX elemental analysis results.

18

3.2. TSL Measurements

Samples were pressed into stainless steel (VA 1.4301) discs and measurments were conducted with a 10-minute delay from 20 to 450 °C. Results are shown in Fig. 3. No luminescence signal was registered between 270 and 550 nm.
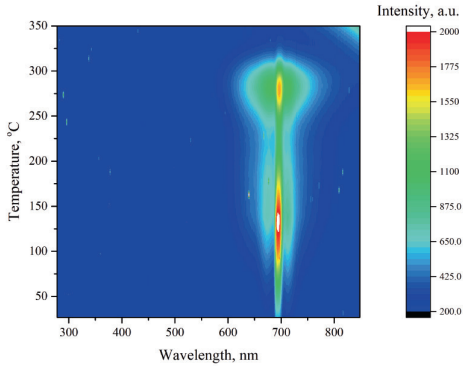
Fig. 3. TSL measurements from 20 to 450 °C with a 10-minute delay after irradiation.
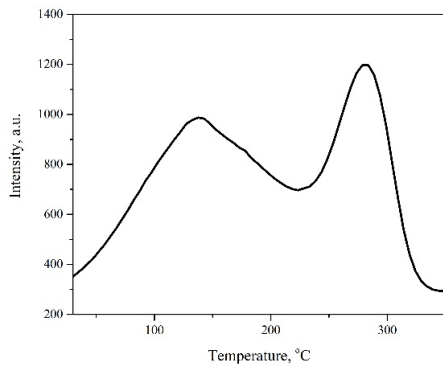
Fig. 4. Relation between the registered TSL intensity and the measured sample temperature heated at 1 K/s.

An example of the registered signal is shown in Fig. 4. Second order approximation summarised in [7] was used to describe the acquired signal (see Fig. 5). Five-peak fit was used and the obtained trap depth energies were as follows: 0.23 eV (1st peak), 0.37 eV (2nd peak), 1.14 eV (3rd peak). All observed glow peaks arise from charge traps at different depths. Peak overlap can contribute to a heating rate, which is enforced by the observations made during fading measurements; over time glow peak intensity fell separately. Peaks are quite direct and one can assume that they could be described adequately with a first-order equation using data from a slower heating rate.

Fig. 5. Results of fitting using Mathematica.

3.3. Dosimetric Properties

To measure material dose response with regard to different types of irradiation, a series of TSL measurments were performed at different irradiation doses. A 30-minute delay before measurements was implemented to avoid registering sample afterglow. Signal was registered through a quartz window without a slit or a filter.

The first (67 °C) and second (157 °C) peaks faded almost completely after 24 hours, which was undesirable for dosimetric applications. The third peak at 286 °C was used to determine the relation between the irradiation dose and the registered TSL signal (see Fig. 6).

19
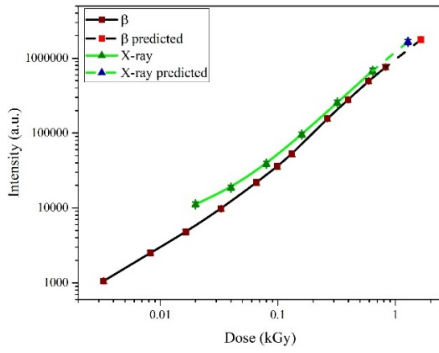
Fig. 6. Relation between the irradiation dose and the registered TSL signal.

Linear fit poorly approximated the relation between the irradiation dose and the registered signal intensity from 3.3 Gy to 1.65 kGy with of 0.86 and reduced Chi-Sqr of 21.38. Data points were closer represented with a parabolic function with of 0.99 and reduced Chi-Sqr of 0.9. They will be further iterated during discussion.

TSL signal fading was measured up to 31 days. The results are shown in Fig. 7; black points represent the relation between the registered intensity and days elapsed, and red points represent the percentage of charge retained in respect to a measurement preformed right after irradiation. Samples were exposed to 1200 s (66 Gy) of beta irradiation because it was the midpoint of a logarithmic exposure range.

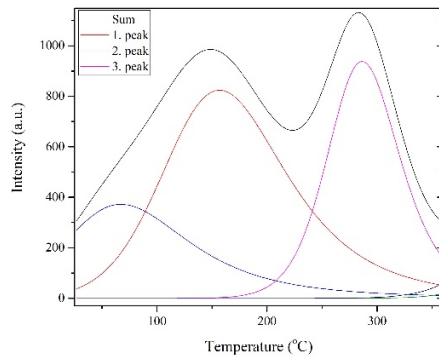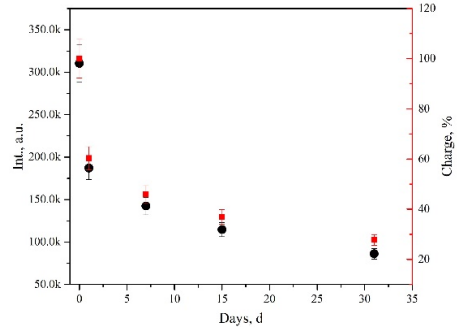Fig. 7. Relation between days after exposure to beta radiation and the registered TSL signal. Black points represent the measured intensity and red points represent the remaining charge.

4. DISCUSSION

Our previous research [6] proposed chromium (III) doped alumina as a good candidate for high dose applications. The aim of this research has been to reproduce the previously acquired results with adequately calibrated equipment and expand using the acquired data. The fact that alumina displays a growing parabolic relation between TSL intensity and the dose it was exposed to only furthers the narrative that chromium doped alumina is a great candidate for high dose dosimetry. Our current equipment forbids substantial and representative exploration of doses above 2 kGy, which proved to be insufficient to achieve saturation or a stark transition between linear and supralinear response regions [8], both of which were usually observable.

Measurements with a higher exposure dosage are required to complete a TSL dose response curve.

While exploring TSL signal fading, a rather harsh drop in intensity was observed as peaks at 67 °C and 157 °C disappeared almost completely after 24 h. High fading for peak at 67 °C was expected due to its rather shallow nature. Rapid discharge of the second glow peak could the attributed to charge transfer between traps, which required further study to prove or disprove. Undoubtedly, during irradiation for 16 h, 32 h and even longer fading would start affecting the TSL signal unpredictably. Usage of stronger beta radiation sources or the determination of discharge rates of R_1, R_2, N and chromium clusters is advised

for further study of the excessive fading. Chromium cluster disintegration due to diffusion is yet to be observed or explored intentionally.

TSL signal reproducibility while using the same sequence and experimental setup was explored. The highest observed intensity deviation was 7.73 %.

5. CONCLUSION

The conducted study has shown that chromium (III) doped alumina displays a promising dose response for use in high-dose applications. Within a margin of error, the material can be used as a linear integral dosimeter from 3.3 to 6.6 Gy and from 9.9 Gy to 1.65 kGy, but saturation was not achieved. A wide high dose linearity range, physical and chemical characteristics, as well as low production costs and ease of synthesis make chromium (III) doped alumina a compelling candidate for applicability as a high dose integral dosimetric material.

In future research, the possibility of conducting OSL measurements for dose determination will be explored.

Chromium (III) doped microceramics displays promising features for dosimetric applications but suffers from considerable fading, which is yet to be fully explored.

ACKNOWLEDGEMENTS

REFERENCES

1. Cardis, E., Gilbert, E. S., Carpenter, L., Howe, G., Kato, I. … & Lave, C. (2006). Effects of Low Doses and Low Dose Rates of External Ionizing Radiation: Cancer Mortality among Nuclear Industry Workers in Three Countries. *Radiation Research*, *142* (2), 117–132. https://doi.org/10.2307/3579020

2. Akselrod, M.S., Kortov, V.S., Kravetsky, D.J., & Gotlib, V. I. (1990). Highly Sensitive Thermoluminescent Anion-Defective. *Radiation Protection Dosimetry*, *32* (1), 15–20.

3. Markey, B. G., Colyott, L. E., & Mckeever, S. W. S. (1995). Time-Resolved Optically Stimulated Luminescence from α-Al$_2$O$_3$:C. *Radiation Measurements*, *24* (4), 457–463. https://doi.org/10.1016/1350-4487(94)00119-L

4. Nikiforov, S. V., & Kortov, V. S. (2014). Dosimetric Response for Crystalline and Nanostructured Aluminium Oxide to a High-Current Pulse Electron Beam.

Radiation Protection Dosimetry, *162* (1–2), 92–95. https://doi.org/10.1093/rpd/ncu225

5. Smits, K., Olsteins, D., Zolotarjovs, A., Laganovska, K., Millers, D., Ignatans, R., & Grabis, J. (2017). Doped Zirconia Phase and Luminescence Dependence on the Nature of Charge Compensation. *Scientific Reports*, *7* (November 2016), 1–7. https://doi.org/10.1038/srep44453

6. Einbergs, E., Zolotarjovs, A., Bite, I., Laganovska, K., Auzins, K. ... & Trinkler, L. (2019). Usability of Cr-Doped Alumina in Dosimetry. *Ceramics*, *2* (3), 525–535. https://doi.org/10.3390/ceramics2030040

7. Kitis, G., Gomez-Ros, J. M., & Tuyn, J. W. N. (1998). Thermoluminescence Glow-Curve Deconvolution Functions for First, Second and General Orders of Kinetics. *Journal of Physics D: Applied Physics*, *31* (19), 2636–2641. https://doi.org/10.1088/0022-3727/31/19/037

8. Horowitz, Y. S. (1984). *Thermoluminescence and thermoluminescent dosimetry* (Volume 2). CRC Press.

COMPARATIVE STUDY ON MICROMECHANICAL PROPERTIES OF ZnO:Ga AND ZnO:In LUMINISCENT CERAMICS

F. Muktepavela[1],*, A. Zolotarjovs[1], R. Zabels[1], K. Kundzins[1],
E. Gorokhova[2], E. Tamanis[3]

[1]Institute of Solid State Physics, University of Latvia,
8 Kengaraga Str., Riga, LV-1063, LATVIA
[2]Scientific and Production Association S.I.Vavilov State Optical Institute,
36 Babushkina Str., Saint Petersburg, 192171, RUSSIA
[3]Daugavpils University,
1 Parades Str., Daugavpils, LV-5401, LATVIA
*e-mail: famuk@latnet.lv

Indium (0.038 at.%) and gallium (0.042 at.%) doped ZnO ceramics were prepared by hot pressing. Ceramics were investigated to determine their structural and mechanical characteristics for the prospective use in scintillators. Based on results of nanoindentation, atom force and scanning electron microscopy as well as energy dispersive X-ray spectra measurements, locations of gallium within grain, indium at grain boundaries (GBs) and their different effect on the mechanical properties of ZnO ceramics were detected. Doping of gallium led to the increased modulus of elasticity in grain, decreased hardness near GBs, stabilization of micropores and brittle intercrystalline fracture mode. ZnO:In ceramic has modulus of elasticity and hardness values close to ZnO characteristics, the increased fracture toughness and some plasticity near GBs. Differences in the micromechanical properties of the ceramics correlate with the location of dopants. Results demonstrate that the ZnO:In ceramic has a greater stress relaxation potential than the ZnO:Ga.

Keywords: Hot pressed ZnO ceramics, microstructure, nanoindentation, fracture mode.

1. INTRODUCTION

ZnO as a wide-band-gap (band gap of 3.37 eV) multifunctional semiconductor possesses excellent luminescent characteristics and is a promising material for scintillators [1]–[3]. With the recent advances in hot press sintering technology, transparent ZnO ceramics based on nanopowders have aroused great interest for the use in fast and high-efficient photo- or X-ray luminescence scintillators [4]. Addition of donor dopants such as Ga or In leads to the improved scintillation characteristics of the ZnO ceramics [5]–[8]. However, the location of dopants in the microstructure is not yet clear. Moreover, despite many studies on the structural and optical properties of the doped ZnO:Ga and ZnO: In ceramics [8], [9], their mechanical characteristics remain practically unexplored even though the modern technology imposes rather strict requirements towards the mechanical properties of brittle optical components as they are subject to vibrations, small mechanical and thermal shock loads. The lack of comparative data on mechanical properties makes it difficult to use these ceramics. Furthermore, mechanical properties are highly structure sensitive [10] and, thus, they can determine not only the technological properties of ceramics, but also the influence of doped elements on the structural-phase state of ceramics. In this regard, as a fast and accurate method to measure the modulus of elasticity and hardness, nanoindentation (NI) is most applicable to ZnO ceramics (in form of thin discs) [11], [12]. NI has been successfully used to detect the mechanical properties of ZnO thin films, single crystals, ceramics and the role of GBs in the fine dispersion materials [13]–[16].

In the present research, the structure, hardness, modulus of elasticity as well as the fracture mode of Ga- (0.042 at.%) and In (0.038 at.%) doped ZnO ceramics are investigated. The aim of the study is to determine the location of dopants in the microstructure of ceramics.

2. EXPERIMENTAL

Commercial zinc oxide powder (Sigma-Aldrich, USA) was used to obtain ceramics. The indium and gallium were introduced in the form of In_2O_3 and Ga_2O_3 by mechanical mixing with the original ZnO powder during 40 min at 293 K [8], [9]. The level of dopants was chosen based on previously studies [9] and corresponded to practically the same scintillation properties of In- and Ga-doped ZnO ceramics. The undoped ZnO, Ga-, and In-doped ZnO ceramics were fabricated by hot uniaxial pressing under vacuum conditions at 1150 °C, 200 MPa for 60 min [4], [9]. The transparent ceramics have been shaped into discs with a diameter of 20–25 mm and a thickness of 1.0–1.5 mm after mechanical processing. The microstructures of etched ceramics surfaces and fracture modes were studied using optical (Nikon, Eclipse L150), atom force AFM (VEECO CP-II) and scanning electron microscopy SEM (TESCAN Lyra 3) equipped with an energy dispersive X-ray spectrometer EDS (Oxford, AZ tec). The nanoindentation station (MTS Nano G200) equipped with a Berkovich-type diamond indenter tip (radius < 20 nm) was used for direct continuous stiffness measuring (CSM), registration of load and displacement, as well as topography imaging.

24

3. RESULTS AND DISCUSSION

3.1. Microstructure of Ceramics

Figure 1 shows the microstructures of the undoped, Ga-, and In-doped ZnO ceramics. The microstructure of undoped ZnO ceramics (Fig. 1a) consists of grains with the grain size of 10–25 μm. The addition of Ga and In changes the microstructure of activated ceramics. Gallium leads to the decrease of the grain size (3–8 μm) without changing the shape of GBs, they remain straight and faceted in places (Fig. 1b, c).
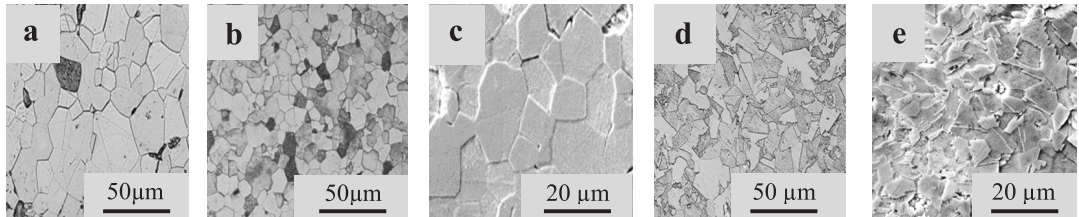
Fig. 1. Optical (a, b, d) and SEM(c, e) images of etched external surfaces of undoped (a), Ga-doped (b, c), and In-doped (d, e) ZnO ceramics.

Indium alters the microstructure more significantly than gallium (Fig.1d, e) changing the shape of both grains and GBs: fine grains are irregular, elongated, some faceted grains have size of 8–12 μm, and a serrated shape of GBs appears. A similar influence of indium on the GBs shape in the ZnO ceramics based on different ZnO powders was described in [8]. Faceted straight GBs for the mechanical properties are the paths for the easy propagation of cracks. However, the presence of the serrated GBs in the ZnO:In ceramics prevents the rapid spread of cracks along GBs [10].

3.2. Nanoindentation of ZnO:Ga and ZnO:In Ceramics

To study the differences in the mechanical behaviour, it was necessary to carry out measurements on individual grains at different loads. Under low loads, the hardness values in the individual grain by the movement of structural defects are determined. Under higher loads when the size of deformation zone exceeds the size of grain, the hardness is affected by properties of GBs [11], [12], [16]. As it is known, according to the Berkovich hardness formula $H = 2.092\frac{P}{a^2}$, where P – load, a – side of Berkovich indenter imprint, indentation depth h is calculated as $h = a/7.7$. The size of the deformation zone around the imprint can be estimated as $t = n{\cdot}a$, for oxide systems a value of the coefficient n of 1.5 can be assumed [12].

Figure 2 shows the hardness and modulus of elasticity *vs* indentation depth for ZnO:Ga and ZnO:In ceramics. Results showed the presence of hardness size effect for both ceramics. However, this effect is expressed in a different range of indentation depths compared to ZnO single crystal [14], [15]. In order not to take into account

the influence of both size effect and nano-heterogeneity of the relief, the results

starting from a depth of 50–100 nm will be considered.
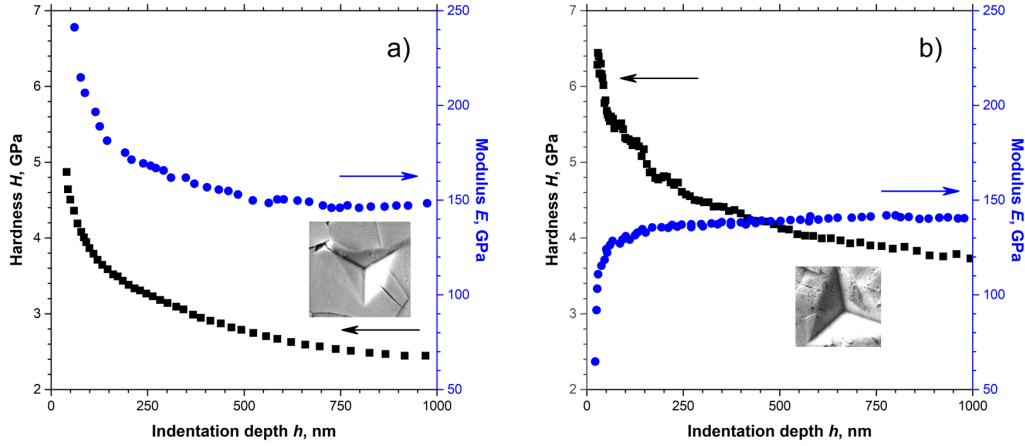
Fig. 2. Hardness, H (■) and modulus of elasticity, E (●) *vs*. indentation depth: ZnO:Ga (a) and ZnO:In (b) ceramics. The inserts show SEM images of indentation induced cracking at large loads: (a) in ZnO:Ga and (b) in ZnO:In.

In the ZnO:Ga ceramics (Fig. 2a) at depth of 100 nm, the deformation zone of 1.16 μm is smaller than the grain size (3–8 μm). The hardness values inside the grain are around 4.0–4.5 GPa ($\pm$0.3 GPa), which is consistent with those for the single crystal or within grain in undoped ZnO ceramics. At depth of 600 nm when deformation zone is more than 8.0 μm and more grains become included into the deformation process, the hardness values decrease to 2.5 GPa. As it can be seen from the inserts in Fig. 2a, the drop in the hardness values is accompanied with the development of cracks (with length C $\geq$ 10 μm) around the imprint, indicating the brittleness of GBs in the ZnO:Ga ceramics. At the same time, the average value of modulus of elasticity at the depth of 100–250 nm inside the grains (175 $\pm$ 2 GPa) is higher compared to that for undoped ZnO single crystal, where E = 140–144 GPa [14]. As it is known, the elastic modulus is almost insensitive to the grain size, but it is rather sensitive to the presence

of additive elements and compounds in the microstructure [10]. Therefore, an increase in the elastic modulus indicates a change in the structural-phase state of the grain, which can be associated with the presence of a ZnO-based solid solution with a low concentration of the ZnO(Ga) compound. This is indirectly confirmed by the data on the modulus of elasticity of gallium oxide (170 GPa) obtained in [16]. The presence of gallium inside the grain is also consistent with the data of ZnO:Ga ceramic microstructure given above where, as seen from Fig. 1b, c, gallium refines grains without GBs modification.

The loading experiment for the ZnO:In ceramics was carried out both at the centre of a large grain with size of 8–12 μm and near GBs. As it is apparent from Fig. 2b, the hardness values at the depth of 100 nm when the deformation zone is inside an individual grain are 4.5–5.0 GPa and slowly decrease to the values of 4.2 GPa when approaching the GBs at the indentation depth of 400–500 nm. Thus,

the influence of GBs on the hardness in this case is not high compared to that of the ZnO:Ga ceramics. Moreover, at the depth of 1000 nm, where the deformation zone of 11.5 μm considerably exceeds the grain size, the hardness value of 3.8 GPa remains higher compared to the ZnO:Ga ceramics. The modulus for the ZnO:In ceramics did not have high values within the grains remaining at the level of 140 GPa.

To elucidate the features of the GBs, similarly to the above-mentioned measurements for the centre of the grain, NI measurements were performed directly near the GBs: 1.5 μm away from a randomly selected GB. In this case, the hardness values were around 3.2 GPa and they generally remained constant at the depth of 2000 nm, exhibiting no signs of long brittle cracks around the imprint. Only a narrow crack with the length C = 3.0 μm could be seen (Fig. 2b).

SEM images (see insets in Fig. 2a, 2b) and the data obtained above made it possible to estimate the values of fracture toughness by indentation (K_{1c}) for investigated ceramics using the formula $K_{1c} = 0.016 \, (E/H)^{1/2} \, P/C^{3/2}$ [17], where E – modulus, H – hardness, P – load, C – crack length. Assessments received were: K_{1C} = 1.12 MPa m$^{1/2}$ and K_{1C} = 2.5 MPa m$^{1/2}$ for ZnO:Ga and for ZnO:In, respectively. Thus, indentation toughness of the ZnO:In ceramics is higher than that of ZnO:Ga ceramics, which is due to the peculiarities of the GBs properties.

To visualize the unusual behaviour of GBs in the ZnO:In ceramics, measuring the height profile across the imprint placed directly near the GBs was performed.

As it is apparent from Fig. 3, the height of the piled-up material near the GB is double the height on the opposite side, which indicates plastic deformation and stress relaxation at GBs in the ZnO:In ceramics.

Fig. 3. AFM topography image and height profile across the imprint of the Berkovich pyramid located close to a GB in the ZnO:In ceramics.
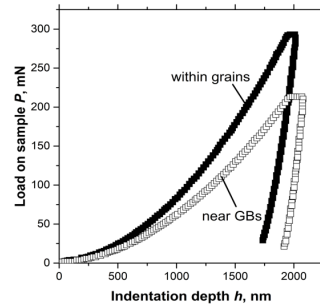
Fig. 4. Loading – unloading curves at indentation on grain and near the grain boundary vs. indentation depth for the ZnO:In ceramics.

To confirm this hypothesis, let us analyse the loading curves for two cases: (i) when deformation is localised within grains and (ii) when deformation occurs near GBs. The loading – unloading curves (Fig. 4) revealed differences for these two groups. The calculated work of plastic deformation during NI, according to [19], shows a

greater value near the GBs in comparison with the bulk of the grain: 81 % and 91 %, respectively. Thus, the addition of indium oxide leads to the appearance of some GB plasticity in ZnO:In ceramics. The influence of dopants on the GBs properties in ZnO varistors is well known and is related to the segregation of the doping metallic elements

at GBs [20]. This is the so-called "metallization" phenomenon, which is unwanted in varistors because it greatly reduces the electrical resistance of the ZnO ceramics. In the case of mechanical properties, the presence of indium at GBs is favourable, as it eliminates the GB brittleness.

3.3. Fractography and EDS Data

Fracture surfaces of the samples were investigated using SEM and EDS methods.

Data of fracture mode of undoped, ZnO:In and ZnO: Ga ceramics are presented in Fig. 5.
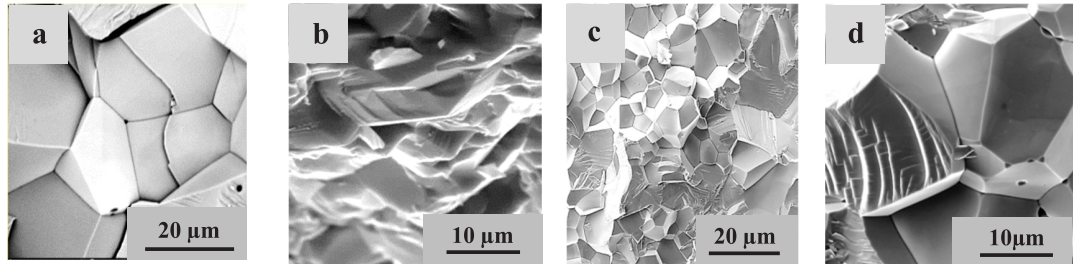
Fig 5. SEM images of the fracture surfaces in undoped (a),
In-doped (b) and Ga-doped (c, d) ZnO ceramics.

As it is apparent from the SEM images, the undoped ZnO ceramics (Fig. 5a) mainly exhibits brittle intergranular fracture. Cracks and micropores are visible. The introduction of indium completely changes the mechanism of ZnO ceramics fracture. As seen in Fig. 5b, the ZnO:In ceramics has transcrystalline fracture mode. Stretched grains and the contours of GBs without micropores or crack were possible to detect.

On the contrary, the fractographs of the ZnO:Ga ceramics demonstrate heterogeneous microstructure and brittle intercrystalline fracture mode (Fig. 5c, d). Small micropores with size of 0.1–0.2 μm on the GBs and in the grains are present in this material. This result confirms the impossibility of vacancy dissolution of pores in the case when the size of pores is much less than the distance (5–8 μm) between sources (in grains) and sinks of vacancies on GBs [20]. The rounded shape of micropores in the grain and triangular shape at the triple joints of GBs indicate the role of micropores as vacancy sinks [21].

The EDS measurements were conducted on the fracture surfaces to determination the relative ratio of Zn/O in the grains and at the GBs for Ga- and In-doped ZnO ceramics (Fig. 6). Gallium was not detected due to its low concentration and low atomic number, which is 31, compared to indium number, which is 49. EDS data for ZnO:In ceramics clearly demonstrate at GBs (Fig. 6b).

Let us consider the obtained EDS values for ceramics in detail compared to single ZnO crystal where Zn/ O ratio is 49.94:50.06 at.%

For ZnO:In ceramic, as it is seen in Fig. 6a, grains in core are enriched with oxygen, but amount of Zn is reduced; in places with numerous GBs (Fig. 6b), the GBs are enriched with Zn and indium but depleted in oxygen.

In the ZnO:Ga ceramics (Fig. 6c), grains are enriched with Zn and depleted with oxygen, but in the grain groups, where the ratio was 47.02:52.98 (at.%), GBs were enriched with oxygen but depleted with Zn.
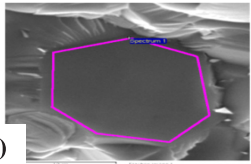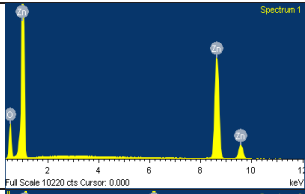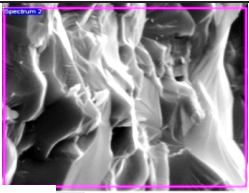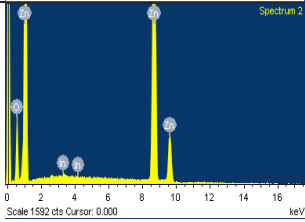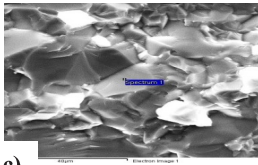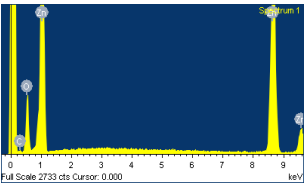
Structure	EDS spectra	Elements, at%
a)		ZnO :In, big grain Zn K | 44.70 O K | 55.30
b)		ZnO :In, GBs Zn K | 57.1 O K | 42.6 In K | 0.17
c)		ZnO :Ga, grains, Zn K | 58.47 O K | 41.53

Fig. 6. ZnO ceramics structure, EDS spectra and ratio of elements:
a) ZnO:In, big grain, b) ZnO:In, places with GBs, c) grains and GBs in ZnO:Ga.

A comparison of the EDS results revealed a general regularity; namely, the location of the dopants in the microstructure was accompanied by a high content of zinc and a low content of oxygen. Therefore, the ratio Zn/O reflects also the accumulation of interstitial zinc ions under the conditions when gallium or indium substitutes zinc.

The formation of a solid solution on ZnO base is quite realistic, since the data of XRD always indicated only the wurtzite as the based structure at low impurity concentrations [3], [9]. Interstitial ions as shallow donors give rise to a number of free electrons and play an important role in the enhancement of exciton band in the luminescence spectrum of ZnO:In and ZnO:Ga ceramics [6], [7], [22]. On the other hand, interstitial zinc ions can actively participate in diffusion during ceramics sintering, which at the last stages is controlled by grain boundary diffusion [23]. This is also confirmed by the data given in [24], where the activation energies of surface (Q_{surf}), grain boundary

(Q_{gb}) and volume (Q_v) diffusion for ZnO ceramics were estimated as 158, 282 and 376 kJ mol^{-1}, respectively. In contrast to the optical properties, the effect of indium and gallium on the structural and mechanical properties of ceramics is different, as can be seen from the results obtained. In this case, sintering and diffusion processes play an essential role in the formation of microstructure and mechanical properties.

From this point, the presence of ZnO(Ga) compound and Zn interstitial ions into grains lead to the stabilization of micropores both inside the grain and at the GBs in ZnO:Ga ceramics (Fig. 5c, d). There are no favourable conditions for healing of pores during hot pressing since the both pressure (0.2 GPa) and temperature 1150 °C (0.6 T_m) are incommensurably small for the required pressure (175 GPa) and for volume diffusion (0.9 T_m) in grains. It is also impossible to heal micropores by dissolving and emitting vacancies. As shown above (Fig. 5), they can be sinks for vacancies, which,

on the one hand, is very positive for luminescent properties, but on the other hand, it leads to increased brittleness of the ZnO:Ga ceramics.

The results obtained showed that, in contrast to gallium, indium was located at grain boundaries in the microstructure of ZnO:In ceramics (Fig. 6b). This leads to the active participation of interstitial ions both in the sintering processes and in the modification of the GB structure. These factors contribute, as shown above, to a decrease in mechanical stresses, as well as to the appearance of some plasticity in ZnO:In ceramics.

3. CONCLUSIONS

Hot pressed indium (0.038 at.%) and gallium (0.042 at.%) doped ZnO ceramics have been studied to determine their structural and micromechanical characteristics. The use of nanoindentation, structural and EDS methods have made it possible for the first time to detect the location of Ga inside grains, indium at GBs in the microstructure, as well as their different effect on the mechanical properties of ceramics.

The ZnO:Ga ceramics is characterised by the increased values of the elastic modulus (175 GPa) inside grain, decreased hardness (2.5 GPa) near GBs and intergranular brittle fracture mode due the presence of stable micropores. ZnO:In ceramics has modulus of elasticity and hardness values close to ZnO characteristics, transcrystalline fracture mode, increased indentation toughness and some plasticity near GBs.

The differences in the properties of the studied ceramics correlate with the location of dopants and are caused by a different behaviour of Ga and In during sintering processes.

As the main result, the ZnO:In ceramics has a greater mechanical stress relaxation potential than the ZnO:Ga ceramics. This finding is very important for the use of ZnO:In ceramics as materials for scintillator.

REFERENCES

1. Ozgur, U., Alivov, Y. I., Liu, C., Teke, A., Reshchikov, S. … & Morkoc, H. (2005). A Comprehensive Review of ZnO Materials and Devices. *Journal of Applied Physics, 98,* 043011.

2. Yan, T., Trinkler, L., Korsaks, V., Lu, C. Y., Berzina, B. ... & Ploog, K. H. (2020). Anisotropic Photoluminescence of Nonpolar ZnO Epilayers and ZnO/Zn1−xMgxO Multip-le Quantum Wells Grown on LiGaO$_2$ Substrate. *Optic Express*, *28* (4), 5629–5638.

3. Grigorjeva, L., Miller, D., Grabis, J., Monty, C., Kalinko, A. .... & Lojkowski, W. (2008). Luminiscence Properties of ZnO Nanocrystals and Ceramics. *IEEE Transactions on Nuclear Science, 55*, 1551–1555.

4. Rodnyi, P. A., Chernenko, K. A., Gorokhova, E. I., Kozlovskii, S. S., Khanin, V. M., & Khodyuk, I.V. (2012). Novel Scintillation Material – ZnO Transparent Ceramics. *IEEE Transactions on Nuclear Science*, *59* (5), 2152–2155.

5. Wilkinson, J., Ucer, K. B., & Williams, R. T. (2005). The Oscillator Strength of Extended Exciton States and Possibility for Very Fast Scintillators. *Nuclear Instruments and Methods in Physics Research, A., 537*, 66–70.

6. Makino, T., Segawa, Y., Yoshida, S., Tsukazaki, A., Ohtomo, A., & Kawasaki, M. (2004). Gallium Concentration Dependence Of Room Temperature Near-Band-Edge Luminescence in n-Type ZnO:Ga. *Applied Physics Letters*, *85* (5), 759–761.

7. Kano, M., Wakamiya, A., Sakai, K., Yamanoi, K., Cadatal-Raduban, M. ... & Fukuda, T. (2011). Response-Time-Improved ZnO Scintillator by Impurity Doping. *Journal of Crystal Growth*, *318* (1), 788–790.

8. Muktepavela, F., Maniks, J., Grigorjeva, L., Zabels, R., Rodnyi, P., & Gorokhova, E. (2018). Effect of In Doping on the ZnO Powders Morphology and Microstructure Evolution of ZnO:In Ceramics as Material for Scintillators. *Latvian Journal of Physics and Technical Sciences, 55* (6), 35–42.

9. Chernenko, K. A., Gorokhova, I., Erońko, S. B., Sandulenko, A., Venevtsev, I. D. ... & Rodnyi, P. (2018). Structural, Optical and Luminescent Properties of ZnO:Ga and ZnO:In Ceramics. *IEEE Transactions on Nuclear Science, 65* (8), 2196–2202.

10. McLean, D. (1977). *Mechanical properties of metals*. Krieger Publishing Company.

11. Fisher-Cripps, A.C. (2002). *Nanoindentation*. NY. Springer.

12. Gouldstone, A., Koh, H. J., Zeng, K. Y, Giannakopoulos, A. E., & Suresh, S. (2000). Discrete and Continuous Deformation during Nanoindentation of Thin Films. *Acta Materialia, 48* (9) 2277–2295.

13. Ivor, M., Medved, D., Vojtko, M., Naughton-Duszova, A., Marciniak, L., & Dusza, J. (2020). Nanoindentation and Tribology of ZrB$_2$ Based Luminescent Ceramic. *Journal of European Ceramics Society, 40* (14) 4901–4908.

14. Zabels, R., Muktepavela, F., Grigorjeva, L., Tamanis, E., & Mishels-Piesins, M. (2010). Nanoindentation and Photoluminescence Characterization of ZnO Thin Films and Single Crystals. *Journal of Optical Materials*, *32* (8), 818–822.

15. Muktepavela, F., Bakradze G., & Sursaeva, V. (2008). Micromechanical Properties of Grain Boundaries and Triple Junctions in Polycrystalline Metals Exhibiting Grain Boundary Sliding at 293K. *Journal of Materials Science, 43* (11) 3848–3854.

16. Pearton, S. J., Yang, J., Cary, P. H. IV., Ren, F., Kim, J. … & Mastro, M., A. (2018). A Review of Ga$_2$O$_3$ Materials, Processing, and Devices. *Applied Physics Review, 5* **(**1), 011301.

17. Gong, J., Wang, J., & Guyan, Z. (2002). Indentation Toughness of Ceramics: A Modified Approach. *Journal of Materials Science, 37*, 865–869.

18. Yonenaga, I. (2005). Hardness, Yield Strength and Dislocation Velocity in Elemental and Compound Semiconductors. *Materials Transaction, 46* (9), 1979–1985.

19. Milman,Yu. V., Galanov, B. A., & Chugunova, S. I. (1993). Plasticity Characteristics Obtained through Hardness Measurement. *Acta Metallurgica et Materialia,* 41 (9), 2523–2532.

20. Nahm, C. W., & Park, C. H. (2000). Microstructure, Electrical Properties, and Degradation Behavior of Praseodymium Oxides-Based Zinc Oxide Varistors Doped with Y$_2$O$_3$. *Journal of Materials Science, 35* (12), 3037–3042.

21. Muktepavela, F., & Maniks, J. (2003). Interface Diffusion Controlled Sintering of Atomically Clean Surfaces of Metals. *Defects and Diffusion Forum*, *216–217*, 169–174.

22. Kelly, J.P., & Graeve, O. A. (2012). Effect of Powder Characteristics on Nanosintering Mechanisms of Convention Nanodensification and Field Assisted Processes. *Sintering*. Springer, Berlin, Heidelberg, 57–95.

23. Vorobyeva, N. A., Rumyanceva, M. N., Forsh, P. A., & Gaskov, A. M. (2013). Conductivity of Nanocrystalline ZnO(Ga). *Semiconductors, 47* (5), 650–564.

24. Ewsuk, K. G., Ellerby, D.T., & DiAntonio, C., B. (2006). Analysis of Nanocrystalline and Microcrystalline ZnO Sintering Using Master Sintering Curves. *Journal of American Ceramics Society*, *89* (6), 2003–2009.

25. Huang, G. Y., Wang, C. Y., & Wang, J .T. (2009). Vacancy-Assisted Diffusion Mechanism of Group-III Elements in ZnO: An Ab Initio Study. *Journal of Applied Physics, 105* (7), 073504.

GALLIUM CONCENTRATION OPTIMISATION OF GALLIUM DOPED ZINC OXIDE FOR IMPROVEMENT OF OPTICAL PROPERTIES

A. Spustaka*, M. Senko, D. Millers, I. Bite,
K. Smits, V. Vitola

Institute of Solid State Physics, University of Latvia
8 Kengaraga Str., Riga LV-1063, LATVIA
*e-mail: agnese.spustaka@cfi.lu.lv

The near-band luminescence of doped ZnO is promising for advanced scintillators; however, the dopant type and concentration effects require a detailed study. Undoped and Ga-doped ZnO nanopowders were prepared by a microwave-assisted solvothermal method and the gallium concentration effect on luminescence properties was studied. The near-band luminescence peak position dependence on gallium concentration was observed. Near-band luminescence intensity versus defect luminescence intensity ratio was explored for different gallium concentrations and the optimal value was determined. Samples were prepared with dopant concentrations between 0.2 and 1.5 at%, XRD analysis confirmed that samples contained only zinc oxide hexagonal wurtzite phase. The results of the research showed that ZnO:Ga containing 0.9 at.% gallium was promising for scintillators.

Keywords: *Luminescence, microwave-assisted solvothermal synthesis, optimised concentration, scintillator, ZnO:Ga.*

1. INTRODUCTION

Zinc oxide (ZnO) is a semiconductor material owning a wide band gap (~3.4 eV) and high exciton binding energy (~60 meV), which provides the possibility of observing highly efficient exitonic luminescence even at room temperatures [1]. The applications of zinc oxide are very wide – it is well-known as green, blue-ultraviolet and white-light emitting material, applicable for optoelectronic devices and gas sensors,

catalysts as well as transparent electroconductive windows for solar cells, and many others [2]–[6].

One of the prospective applications is radiation detectors – devices that can detect electromagnetic as well as corpuscular ionizing radiation [7]. Radiation detectors are used in medicine, for example, during positron emission tomography and computer tomography [8], [9]. Moreover, for security and quality control, radiation detectors are used in manufacturing as well as there are other technological applications.

Sharp interest is related to the search for materials applicable for fast operating scintillators. Scintillators are materials for conversion of ionizing radiation photon energy to the light pulse. Thus, scintillators can detect a single ionizing radiation photon or a single charged particle. The ideal scintillator has high stopping power, fast scintillation response, high efficiency for ionizing radiation conversion to light photons, great physical and chemical stability, as well as high radiation hardness. The stopping power of ZnO is good due to large atomic mass of Zn. In turn, the scintillation yield is up to 15 000 photons/MeV [10], scintillation decay time is below 1 ns [10] and ϒ-rays do not create new defects in ZnO crystalline lattice [1]. Therefore, ZnO is a very promising material for advanced scintillators. The two main emission bands in the spectrum of ZnO are the near-band luminescence (NBL) in the near UV range and the defect luminescence band in the visible range. The NBL shows sub-nanosecond decay, whereas defect luminescence decay is within microseconds [11]. The main challenge for fast response scintillators is slow decaying defect luminescence. Therefore, for scintillators it is necessary to have ZnO with intensive NBL and low intensity defect luminescence. The doping of ZnO could suppress the defect luminescence [12], [13]; therefore, the study of doped ZnO is of interest.

There are a large number of reports about undoped zinc oxide; however, the luminescence of ZnO doped with gallium, indium and other dopants is yet to be explored [13]. Doped ZnO powder is a promising material for its usability in producing transparent ceramics with excellent properties for scintillators [14].

Incorporation of dopant, grain size and grain agglomeration of ZnO depends on a synthesis method as well as on chemicals used. Many methods were developed for ZnO synthesis – precipitation, sol-gel, solvothermal, hydrothermal and microwave-assisted solvo- or hydrothermal methods, etc. [15]–[17]. Recently, due to the control of sample morphology and size, temperature gradient versatility, relative simplicity and low reaction times, as well as environmental friendliness, microwave-assisted methods have become more commonly used [18]. On the other hand, incorporation of dopant in ZnO is synthesis dependent and, thus, there is interest in finding the optimal concentration of dopant for each synthesis method.

In the present paper, undoped and Ga-doped zinc oxide were prepared by a microwave-assisted solvothermal (MWST) synthesis technique. The effect of Ga concentration on crystallization, morphology and luminescence properties of ZnO was studied. The optimal gallium concentration with the most efficient NBL and relatively low intensity of defect luminescence was found.

2. EXPERIMENTAL

2.1. Materials

Zinc acetate ($Zn(CH_3COO)_2$, anhydrous, purity 99.9+ %; Alfa Aesar) and sodium hydroxide (NaOH, purity ≥ 98%; Sigma Aldrich) were used as the main precursors for ZnO synthesis; gallium trichloride ($GaCl_3$, purity 99.999 %; Alfa Aesar) was used as a dopant source and ethanol (C_2H_5OH, 96 %; Ltd. Jaunpagasts Plus) – as a solvent. Methanol (CH_3OH, purity ≥99.8 %; Sigma Aldrich) was used for removal of synthesis reaction residue. Analytical grade chemicals were used without any further purification and were used as received.

2.2. Synthesis of Undoped and Ga-doped ZnO Nanomaterials

The undoped and Ga-doped ZnO nanopowders were synthesized by using a microwave-assisted solvothermal method (MWST). The samples of Ga-doped ZnO nanopowders were prepared with eight different concentrations (0–1.5 at.%) of Ga. The MWST reaction was performed in a Milestone synthWAVE microwave reactor in an inert atmosphere (N_2, 99.999 %). The system was operated at 2.45 GHz frequency with power ranging from 0 to 100 % of full power (1.5 kW).

In this synthesis route, the three precursor solutions were prepared by separately dissolving $Zn(CH_3COO)_2$ in ethanol (0.3 M), $GaCl_3$ in ethanol (0.5 M) and NaOH in ethanol (0.6 M) at 80 °C under a constant stirring speed. After all the starting materials were dissolved completely, an appropriate amount of gallium ion solution was added to the 20 mL of zinc ion solution under a constant stirring speed. The solution was stirred for 15 min and after that 20 mL of NaOH solution was slowly added to the metal ion solution under a constant stirring speed. The resulting reaction mixture was stirred for 10 min and a milky white reaction mixture was obtained. After stirring, the reaction mixture was poured into a 70 mL PTFE vial, which was then placed in a Milestone synthWAVE reactor vessel. Undoped ZnO was prepared in the same way without adding a gallium ion solution.
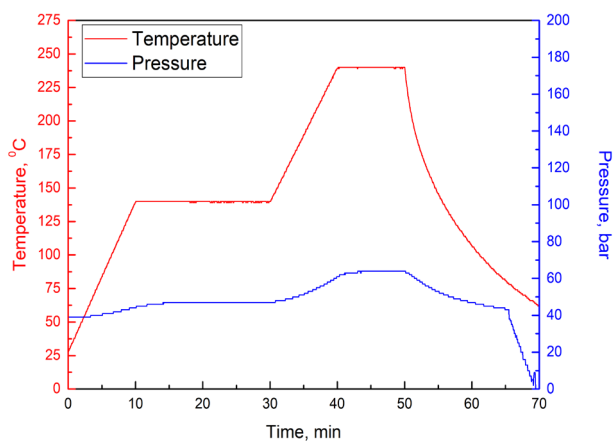

Fig. 1. Profile of MWST synthesis parameters for ZnO nanoparticle preparation.

As shown in Fig. 1, the two-stage synthesis was used to obtain undoped and Ga-doped ZnO. During the synthesis, at the first stage microwave heating ramp was set to be 10 °C/min with the target temperature of 140 °C. At the target temperature, the reaction mixture was irradiated with microwaves for 30 minutes to proceed the complete exchange reaction between precursors, resulting in formation of $Zn(OH)_2$. The starting pressure was set to be 40 bar. The pressure gradually increased by the growing temperature and the increasing amount of gases produced as the reaction by-products. During the second stage, the temperature of 240 °C was achieved in 10 minutes and further the irradiation was continued for 10 minutes. Under these conditions, thermal decomposition of $Zn(OH)_2$ was undergoing. Subsequently, the reaction mixture was naturally cooled down to room temperature. The nanoparticles of ZnO in the resulting sol were separated from the solvent by centrifugation and subsequent washing for 5 times with 20 mL of methanol for 15 minutes. The synthesis of undoped ZnO and ZnO:Ga resulted in white and pastel blue (due to the gallium presence in the sample) coloured powders accordingly.

2.3. Characterisation Techniques

Crystallinity of undoped and gallium-doped zinc oxide samples were characterised by X-ray powder diffraction (XRD) using a Rigaku MiniFlex 600 X-ray diffractometer. Cu Kα radiation was used by setting the cathode voltage to 40 kV and current to 15 mA. The morphology of samples was characterised by scanning electron microscopy (SEM) using a SEM Helios operated at 5 kV. Before the examination, the samples were coated with a thin gold layer.

Photoluminescence (PL) spectral measurements were conducted using a Horiba iHR320 monochromator with 150 l/mm diffraction grating and a blaze wavelength of 500 nm. The monochromator was coupled with an Andor DV420A-BU2 CCD camera. Photoluminescence was excited with a CryLas Nd:YAG laser (266 nm); spot size was approximately 3 mm in diameter, laser impulse duration was less than 2 ns, max repetition rate was 5 kHz with max output power of 0.3 μJ.

3. RESULTS AND DISCUSSION

3.1. X-Ray Diffraction Analysis

X-ray powder diffraction spectra (Fig. 2) show that all peaks of all samples correspond to the hexagonal wurtzite structure. XRD data confirm that no gallium compound impurities are present in samples, meaning that gallium was incorporated in ZnO crystal lattice. Sharpness and relatively high intensity of XRD patterns indicated high crystallinity of powders. Ga-doped ZnO has wider peaks than ZnO and it can take place if ZnO:Ga crystallites are smaller than that for ZnO. A similar impact can be due to larger concentration of defects in ZnO:Ga crystallites. It is known that irradiating material with microwaves produces a greater level of crystallinity than conventional methods, such as wet synthesis [19]. For average crystallite size determination, Debye-Scherrer equation (1) was used:

$$D = \frac{0.9\lambda}{\beta cos\theta},$$ (1)

where λ – X-ray wavelength, β – FWHM, – Bragg diffraction angle.

Grain crystallite sizes of ZnO:Ga samples were found to be in the range of 22–30 nm, with an average being 26 nm. The sizes of crystallites of undoped ZnO were found to be in the range of 39–41 nm. Therefore, wider XRD lines for ZnO:Ga are due to smaller crystallites.
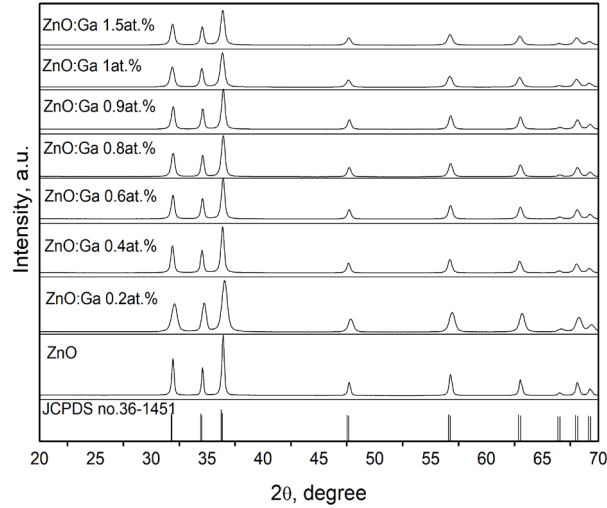
Fig. 2. X-ray powder diffraction patterns for ZnO and ZnO:Ga powders synthesized via MWST method.

3.2. Analysis of SEM Results

Figure 3 shows the morphology of the gallium-doped ZnO nanostructures. The samples appear to be heterogenic (partially due to the presence of gallium in size-able amount). Particle sizes and shapes vary and asymmetrical units can be seen, which suggests partial agglomeration of particles. XRD data showed much smaller crystallite size (~10 times), but the method itself showed the size of individual crystal-lites. SEM image showed that, due to the agglomeration, there might be polycrystal-line grains with different orientations and sizes. The dominant shape appears to be in the form of small nano-rice; there are some particle with greater length, which is due to the polar structure of ZnO and its growth along c-axis.
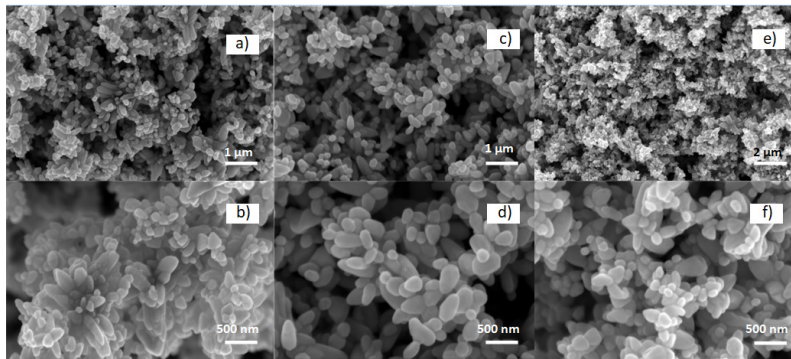
Fig.3. SEM images of ZnO:Ga 0.6 at.% (a,b), ZnO:Ga 0.9 at.% (c, d); ZnO:Ga 1.5 at.% (e,f).

3.3. Luminescence Properties

To compare and study optical properties of samples, powders were fixed in identical holders as well as the placement conditions were the same for all the samples. The repeatability was tested using the same powder fixed in 3 holders; the interchange of these holders showed that the peak positions in luminescence spectra were strongly the same in all cases. The luminescence intensities were reproduced within 10 %; however, the NBL intensity relative to defect luminescence intensity was preserved in all spectra.
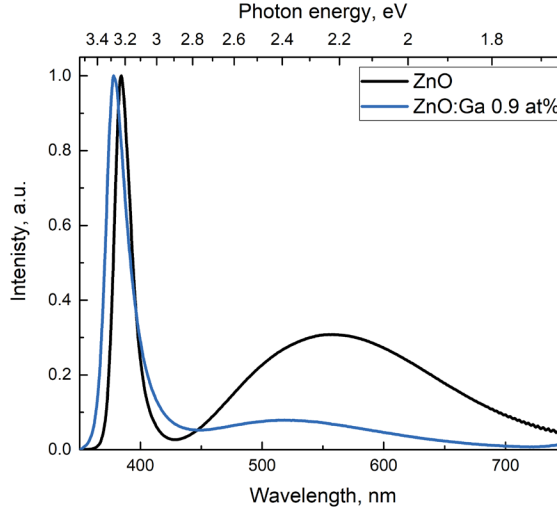
Fig. 4. Comparison of PL spectra of undoped and doped ZnO.

Figure 4 shows room temperature PL spectra of ZnO and ZnO:Ga with 0.9 at%. The spectrum has two main emission bands: a relatively narrow NBL peak and a broad band centred around 550 nm that is attributed to defects in the lattice. The NBL peak positions slightly differ as well as its FWHM. NBL peak position of undoped ZnO is at 384 nm and it is shifted to long wave side. NBL peak position of ZnO:Ga is at 379 nm. It might be due to a wider band gap of ZnO:Ga [20]. The changes in defect luminescence band maximum position could be associated with different luminescence centre contribution to emission. In turn, the relative defect luminescence contribution to undoped ZnO is larger than that for ZnO:Ga. Since the ZnO defect lumines-cence is undesirable for scintillators, the main study focuses on gallium-doped ZnO samples.

Figure 5 shows the photoluminescence spectra for several gallium-doped ZnO samples excited by 266 nm at RT. The spectra exhibit a strong near-band luminesce (NBL) between 377 and 382 nm and a minor peak around 550 nm in the green spectral region, which is also known as defect lumines-cence. One can see that ZnO doping with Ga results not only in the change of intensities of both NBL and defect luminescence but also in relative luminescence intensity. However, it is difficult to determine the best composition for a scintillator from Fig. 5. Therefore, Fig. 6 shows the normalized luminescence spectra.
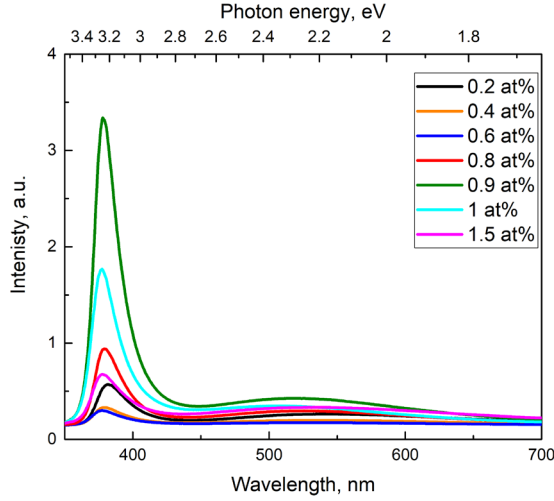
Fig. 5. Photoluminescence spectra of ZnO:Ga with different gallium concentration excited by 266 nm.
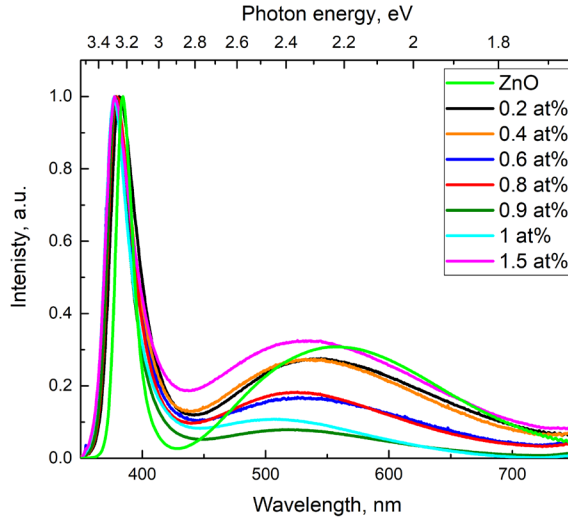
Fig. 6. Normalized photoluminescence spectra of ZnO and ZnO:Ga with different gallium concentration excited by 266 nm.

Figure 6 shows the comparison between luminescence intensity of multiple samples; ZnO:Ga with 0.9 at% displays the relatively low PL intensity in the defect band. The normalized PL spectra clearly show that defect luminescence intensity depends on gallium concentration. Figure 7 illustrates the dependence of the ratio of NBL and defect luminescence intensity (I_{NBL}/I_{def}). Optimal concentration of gallium was determined based on the comparison of NBL peak intensity with defect band luminescence peak intensity. In Fig. 7, the best ratio of NBL intensity and defect luminescence intensity corresponds to 0.9 at% gallium concentration. The error bars are 10 % of result as it could be associated with measurement error to experimentally confirm that samples were synthesized several times and results were repeatable and did not vary more than 10 %.
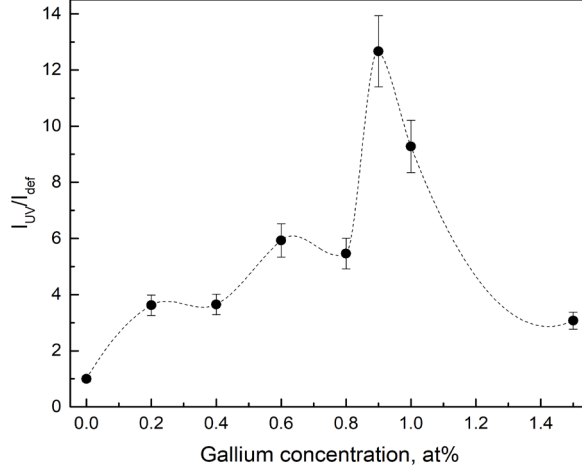
Fig. 7. Optimisation of gallium concentration in ZnO:Ga.

In Fig. 5, it can be observed that NBL peak position slightly differs; Figure 8 shows the dependence of NBL peak position on Ga concentration. The increased concentration results in the peak shift to shorter wavelengths.
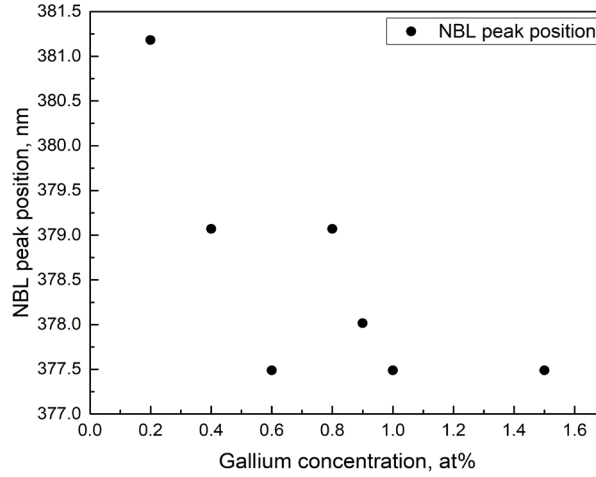
Fig. 8. NBL peak position in PL spectra of ZnO and ZnO:Ga samples.

The study of single crystal NBL luminescence at low temperature showed that there were up to 6 luminescence bands [4]. At RT in NBL, there could be either a free exciton 1 LO phonon replica (Ex1LO), or donor-acceptor pair (DA) luminescence. Intensity of free exciton phonon replicas luminescence of undoped ZnO is strongly reduced at 150 K and position of peak is very close to that for DA [21]. Therefore, the main contribution in NBL at 300 K is from DA. It is known that Ga acts as a donor in ZnO [4] and the peak position of DA luminescence depends on donor and acceptor mutual interaction [22], in other words, on donor–acceptor spatial distribution. There is another possibility that change in the NBL peak position could be associated with a shift of fundamental absorption edge [23]. However, the strong dependence of NBL

on Ga concentration confirms that a donor is involved in the processes responsible for this luminescence.

The change in the defect luminescence band position and shape (Fig. 6) is also noted. These changes demonstrate possible gallium interactions with intrinsic defects in ZnO. Since the intrinsic defect concentration in ZnO is estimated to be at least 10^{18} cm^{-3} [21], even the dopant concentration of 0.2 at% could affect defect luminescence. Large dopant concentration could introduce additional defects necessary for charge compensation.

4. CONCLUSION

Gallium-doped ZnO powders prepared using a micro-wave assisted solvothermal method have wurzite structure and photoluminescence spectra of undoped ZnO and ZnO:Ga samples with concentrations between 0.2 at% and 1.5 at% reveal that near-band luminescence peaking is close to 380 nm and defect luminescence band peak is within the range of approximately 510–550 nm. ZnO:Ga displays an intensive NBL band and a suppressed defect luminescence band, which demonstrates excellent properties for applications in ionizing radiation detectors. Gallium concentration of 0.9 at% presents a relatively very low defect band and high near-band luminescence intensity, which make it a promising candidate for scintillators. This study is also beneficial to understand the influence of gallium concentration on zinc oxide morphology and luminescence properties.

REFERENCES

1. Janotti, A., & van de Walle, C. G. (2009). Fundamentals of Zinc Oxide as a Semiconductor. *Reports on Progress in Physics*, *72* (12). https://doi.org/10.1088/0034-4885/72/12/126501

2. Moezzi, A., McDonagh, A. M., & Cortie, M. B. (2012). Zinc Oxide Particles: Synthesis, Properties and Applications. *Chemical Engineering Journal*, *185–186*, 1–22. https://doi.org/10.1016/j.cej.2012.01.076

3. Mondal, P. (2019). Effect of Oxygen Vacancy Induced Defect on the Optical Emission and Excitonic Lifetime of Intrinsic ZnO. *Optical Materials*, *98* (August), 109476. https://doi.org/10.1016/j.optmat.2019.109476

4. Özgür, Ü., Alivov, Y. I., Liu, C., Teke, A., Reshchikov, M. A. … & Morkọ, H. (2005). A comprehensive Review of ZnO Materials and Devices. *Journal of Applied Physics*, *98* (4), 1–103. https://doi.org/10.1063/1.1992666

5. Procházková, L., Gbur, T., Čuba, V., Jarý, V., & Nikl, M. (2015). Fabrication of Highly Efficient ZnO Nanoscintillators. *Optical Materials*, *47*, 67–71. https://doi.org/10.1016/j.optmat.2015.07.001

6. Wang, Z., Nayak, P. K., Caraveo-Frescas, J. A., & Alshareef, H. N. (2016). Recent Developments in p-Type Oxide Semiconductor Materials and Devices. *Advanced Materials*, *28* (20), 3831–3892. https://doi.org/10.1002/adma.201503080

7. Angub, M. C. M., Vergara, C. J. T., Husay, H. A. F., Salvador, A. A., Empizo, M. J. F. … & Somintac, A. S. (2018). Hydrothermal Growth of Vertically Aligned ZnO Nanorods as Potential Scintillator Materials for Radiation Detectors. *Journal of Luminescence*, *203*, 427–435. https://doi.org/10.1016/j.jlumin.2018.05.062

8. Sato, E., Sugimura, S., Endo, H., Oda, Y., Abudurexiti, A. … & Onagawa, J. (2012). 15Mcps Photon-Counting X-ray Computed Tomography System Using a ZnO-MPPC Detector and its Application to Gadolinium Imaging. *Applied Radiation and Isotopes*, *70* (1), 336–340. https://doi.org/10.1016/j.apradiso.2011.07.002

9. Sato, E., Matsukiyo, H., Osawa, A., Enomoto, T., Watanabe, M. … & Sato, S. (2008). X-ray Computed Tomography System Using a Multipixel Photon Counter. *Hard X-Ray, Gamma-Ray, and Neutron Detector Physics X*, *7079*(2008), 70790H. https://doi.org/10.1117/12.795434

10. Derenzo, S. E., Weber, M. J., Bourret-Courchesne, E., & Klintenberg, M. K. (2003). The Quest for the Ideal Inorganic Scintillator. *Nuclear Instruments and Methods in Physics Research, Section A: Accelerators, Spectrometers, Detectors and Associated Equipment*, *505* (1–2), 111–117. https://doi.org/10.1016/S0168-9002(03)01031-3

11. Grigorjeva, L., Millers, D., Smits, K., Grabis, J., Fidelus, J. … & Bienkowski, K. (2010). The Luminescence of ZnO Ceramics. *Radiation Measurements*, *45* (3–6), 441–443. https://doi.org/10.1016/j.radmeas.2010.03.012

12. Li, Q., Liu, X., Gu, M., Huang, S., Zhang, J. … & Zhao, S. (2016). X-ray Excited Luminescence of Ga- and In-doped ZnO Microrods by Annealing Treatment. *Superlattices and Microstructures*, *98*, 351–358. https://doi.org/10.1016/j.spmi.2016.09.005

13. Kano, M., Wakamiya, A., Sakai, K., Yamanoi, K., Cadatal-Raduban, M. … & Fukuda, T. (2011). Response-Time-Improved ZnO Scintillator by Impurity Doping. *Journal of Crystal Growth*, *318* (1), 788–790. https://doi.org/10.1016/j.jcrysgro.2010.10.192

14. Demidenko, V. A., Gorokhova, E. I., Khodyuk, I. v., Khristich, O. A., Mikhrin, S. B., & Rodnyi, P. A. (2007). Scintillation Properties of Ceramics Based on Zinc Oxide. *Radiation Measurements*, *42* (4–5), 549–552. https://doi.org/10.1016/j.radmeas.2007.01.050

15. al Abdullah, K., Awad, S., Zaraket, J., & Salame, C. (2017). Synthesis of ZnO Nanopowders by Using Sol-Gel and Studying their Structural and Electrical Properties at Different Temperature. *Energy Procedia*, *119*, 565–570. https://doi.org/10.1016/j.egypro.2017.07.080

16. Khoshhesab, Z. M., Sarfaraz, M., & Asadabad, M. A. (2011). Preparation of ZnO Nanostructures by Chemical Precipitation Method. *Synthesis and Reactivity in Inorganic, Metal-Organic and Nano-Metal Chemistry*, *41* (7), 814–819. https://doi.org/10.1080/15533174.2011.591308

17. Ghoshal, T., Biswas, S., Paul, M., & De, S. K. (2009). Synthesis of ZnO Nanoparticles by Solvothermal Method and their Ammonia Sensing Properties. *Journal of Nanoscience and Nanotechnology*, *9* (10), 5973–5980. https://doi.org/10.1166/jnn.2009.1290

18. Thamima, M., & Karuppuchamy, S. (2015). Microwave Assisted Synthesis of Zinc Oxide Nanoparticles. *International Journal of ChemTech Research*, *8* (11), 250–256. https://doi.org/10.1016/j.mspro.2015.11.101

19. Jayathilake, D. S. Y., Peiris, T. A. N., Sagu, J. S., Potter, D. B., Wijayantha, K. G. U. … & Southee, D. J. (2017). Microwave-Assisted Synthesis and Processing of Al-Doped, Ga-Doped, and Al, Ga Codoped ZnO for the Pursuit of Optimal Conductivity for Transparent Conducting Film Fabrication. *ACS Sustainable Chemistry and Engineering*, *5* (6), 4820–4829. https://doi.org/10.1021/acssuschemeng.7b00263

20. Makino, T., Segawa, Y., Yoshida, S., Tsukazaki, A., Ohtomo, A., & Kawasaki, M. (2004). Gallium Concentration Dependence of Room-Temperature Near-Band-Edge Luminescence in n-Type ZnO:Ga. *Applied Physics Letters*, *85* (5), 759–761. https://doi.org/10.1063/1.1776630

21. Meyer, B. K., Alves, H., Hofmann, D. M., Kriegseis, W., Forster, D. … & Rodina, A. V. (2004). Bound Exciton and Donor-Acceptor Pair Recombinations in ZnO. *Physica Status Solidi (B) Basic Research*, *241* (2), 231–260. https://doi.org/10.1002/pssb.200301962

22. Kotomin, E. A., & Doktorov, A. B. (1982). Theory of Tunneling Recombination of Defects Stimulated by their Motion II. Three Recombination Mechanisms. *Physica Status Solidi (B)*, *114* (2), 287–318. https://doi.org/10.1002/pssb.2221140202

23. Kim, J., Naik, G. V., Gavrilenko, A. V., Dondapati, K., Gavrilenko, V. I. … & Boltasseva, A. (2014). Optical Properties of Gallium-Doped Zinc Oxide – A Low-Loss Plasmonic Material: First-Principles Theory and Experiment. *Physical Review X*, *3* (4), 1–9. https://doi.org/10.1103/PhysRevX.3.041

PEROVSKITE CH$_3$NH$_3$PbI$_{3-X}$Cl$_X$ SOLAR CELLS AND THEIR DEGRADATION (PART 1: A SHORT REVIEW)

I. Kaulachs*,[1,2], A. Ivanova[2,3], A. Tokmakov[1],
M. Roze[3], I. Mihailovs[1,3], M. Rutkis[1]

[1] Institute of Solid State Physics, University of Latvia,
8 Ķengaraga Str., Riga, LV-1063, LATVIA
[2] Institute of Physical Energetics,
11 Krīvu Str., Riga, LV-1006, LATVIA
[3] Institute of Applied Chemistry, Riga Technical University,
3 Paula Valdena Str., Riga, LV-1048, LATVIA

Development of hybrid organic-inorganic perovskite solar cells (PSC) has been one of the hottest research topics since 2013. Within brief literature review, we would like to achieve two objectives. Firstly, we would like to indicate that a whole set of physical properties, such as high change carrier mobility, very low recombination rates, large carrier life time and diffusion length, large absorption coefficients and very weak exciton binding energies, are defining high power conversion efficiency (PCE) of methyl ammonium lead trihalide SC. The second objective is to draw attention to some, in our opinion, important aspects that previously have not been satisfactory addressed in literature. Although degradation of PSC is widely discussed, processes at very first exposure to ambient conditions after deposition of top electrode are uncovered.

Keywords: *Inverted solar cells, lead halide perovskite, power conversion efficiency.*

1. INTRODUCTION

Due to the increasing demand for clean energy, much research effort has been dedicated to the improvement of solar energy technologies. As a result, in 2013 Grätzel's group created a mesoporous hybrid organic-inorganic perovskite solar cell (PSC) with certified power conversion efficiency (PCE) of 15 % [1]. At the same time, Snaith's group also succeeded in creating a planar organic-inorganic perovskite solar cell with PCE of

15.4 % [2]. In the prominent scientific journal "Nature", these PSCs were described as one of the ten greatest scientific achievements of 2013 [3]. Since the time of these achievements, the research into PSCs has grown rapidly, which has been described as a "perovskite fever" [4], and in 2019 the efficiency of the PSCs reached 24.2 % [5].

These astonishing efficiencies are attributed to the very interesting electronic and optical properties of the perovskite layer [6]–[13]. The most studied compound for the perovskite solar cells is methyl ammonium lead triiodide ($CH_3NH_3PbI_3$). It has a charge carrier mobility of 8 cm^2/(V·s) in thin polycrystalline layers [6], but this quantity is much higher for monocrystals, reaching 105±35 cm^2/(V·s) [13]. These perovskites also have extremely low charge carrier recombination rates for both the monomolecular and the bimolecular recombinations [6]. In addition, they feature an ambipolar charge transport with a balanced electron and hole diffusion lengths, these being greater than 100 nanometers in a polycrystalline $CH_3NH_3PbI_3$ layer [14], [15]. In monocrystals, though, the electron and the hole diffusion lengths exceed 175 μm under illumination of nominal full sunlight intensity and even 3 mm under 1000 times weaker illumination [13]. The aforementioned features of trihalide perovskites provide long lifetime of photogenerated charge carriers [6], [11], [14], [16]. These perovskites have a broad absorption spectrum covering all the visible range up to 800 nm on the red side, with a high absorption coefficient from $5 \cdot 10^4$ up to $5 \cdot 10^5$ cm^{-1} [17]–[20]. Commonly, a thickness of 300÷400 nm is sufficient for such a perovskite to fully absorb the incident visible light [18], [21], [22].

2. DISCUSSION

It is possible to create exceptionally thin solar cells with a record power-per-weight figure of merit of 23 W·g^{-1} [22], which was never achieved by any other competing photovoltaic technologies. Another advantage is the low fabrication cost of such solar cells, "because material cost of the $CH_3NH_3PbI_3$ absorber (300 nm thick) is less than US$ 2 per square meter and the coating processes are very simple" [18]. These cells do not have excitonic nature, unlike the organic solar cells, but rather have photoexcitations spontaneously dissociating into free carriers in the bulk of the junction, as in the inorganic cells [23]. This characteristic is determined by the very small exciton binding energy of ~ 2 meV [24] and high static dielectric constant $\varepsilon \sim 70$ [24]. These very low exciton binding energy values were also confirmed by other groups, namely, 6 meV [25], [26] at the room temperature for high-quality metal-organic triiodide perovskite layers obtained by the interdiffusion method; a somewhat higher value of ~ 22÷24 meV was found by optical spectroscopy using Elliott analysis [27]. This explains the very impressive performance of the metal-organic perovskite solar cells: following the absorption of the light, the free charge carriers are generated spontaneously.

Although the triiodide perovskites are the most widely investigated ones, usage of a mixed halide perovskite $CH_3NH_3PbI_{3-x}Cl_x$ as light absorber has some advantages, as it has much higher charge carrier mobilities and diffusion lengths even in polycrystalline layers (up to 1μm, which is an order of magnitude higher than for the pure iodide perovskite) [11]. The Cl$^-$ presence in the

perovskite precursor solution improves the layer crystallization and increases the charge carrier lifetime up to 1μs [12], [20]. The mixed halide perovskites also have higher PCE values and are more stable [28]. Despite the content of chlorine in the $CH_3NH_3PbI_{3-x}Cl_x$ is very small and x does not exceed 2÷4 % [12], [20], [29], it decreases concentration of the bulk traps by about an order of magnitude compared to the $CH_3NH_3PbI_3$ [30], [31]. The chlorine additive alters the direction of the grain growth for perovskite layers formed from the precursor solution in DMF on PEDOT:PSS-covered indium-tin oxide (ITO) glass, so that the $CH_3NH_3PbI_3$ forms a fibrous structure with a low surface coverage, whereas the $CH_3NH_3PbI_{3-x}Cl_x$ tends to crystallize in a planar fashion with a practically complete substrate coverage [30].

Another option for obtaining the highest power conversion efficiencies is mesoporous bulk heterojunction cells; these, however, typically contain expensive charge-transport-and-blocking layers, which need high-temperature (400÷500 °C) [32]–[34] sintering, thus increasing the processing time and the cost of the solar cell. To overcome these drawbacks, a low-temperature-processed inverted planar p|i|n solar cell could be produced using poly(3,4-ethylene-dioxythiophene) poly(styrenesulphonate) (PEDOT:PSS) as the hole-transport (p) and electron-blocking layer material, while the phenyl-C_{61}-butyric acid methyl ester (PCBM or, more specifically, $PC_{61}BM$) is employed in the electron transport (n) layer (ETL), as frequently done in the design of planar inverted hybrid solar cells [28], [35], [44]–[46], [36]–[43]. These charge-carrier transport layers are also applicable to the low-cost printable or roll-to-roll manufacturing solar cells [47].

Usually after PCBM is spin-coated onto a perovskite film, the traps are efficiently passivated and their density in the cell is decreased by nearly two orders of magnitude within the 0.4÷0.5 eV range; photocurrent hysteresis is also diminished [48], [49]. The shallow trap states in the 0.35÷0.40 eV range, however, are passivated only after thermal annealing of the PCBM layer for 45 min at 100 °C [48]. The hole mobility in the plane direction has also been reported to increase up to 114 cm²/(V·s) for a polycrystalline perovskite film covered by PCBM layer [48]. This means that after thermal annealing, the PCBM diffuses into the perovskite layer along the grain boundaries, passivating the shallow trap states there and reducing the energy barrier between the grains, which enhances the hole transport in the plane direction [48]. Even better trap passivation has been achieved when the PCBM layer is covered with a C_{60} layer. Such a bilayer ETL can passivate not only the shallow trap states but also the ones deeper than 0.5 eV [50], and it also reduces the dark current by 3÷4 orders of magnitude.

Despite the attractive performance and the low fabrication cost of organic-inorganic perovskite solar cells, the long-term stability is a major drawback hindering their practical application [28], [44], [51]–[57]. These cells degrade rapidly under humid air, sunlight and heat [51]–[58]. Among these causes, humidity is the main as it significantly amplifies the degradation speed of the cell under oxygen, light and temperature after reaching a threshold of $2 \cdot 10^{10}$ langmuir of water vapour exposure [58]–[60]. It was shown that moisture permeates into the polycrystalline perovskite $MAPbI_3$ layer through the grain boundaries much more quickly than reacts with the grain top surface, as the grain boundaries consist of a ~5 nm thick amorphous intergranual film [61]. The degradation process proceeds in two stages. At first, the perovskite mono-

hydrate $CH_3NH_3PbI_3 \cdot H_2O$ and also the mixed dihydrate are formed, which are fully reversible reactions, the direction of which depends on the water vapour concentration in air [53, 57, 60, 61]:

$$CH_3NH_3PbI_3 + H_2O \rightleftarrows CH_3NH_3PbI_3 \cdot H_2O \tag{1a}$$

$$3CH_3NH_3PbI_3 + CH_3NH_3PbI_3 \cdot H_2O + H_2O \rightleftarrows (CH_3NH_3)4PbI_6 \cdot 2H_2O + 3PbI_2 \tag{1b}$$

$$(CH_3NH_3)_4PbI_6 \cdot 2H_2O \rightleftarrows 4CH_3NH_3I + PbI_2 + 2H_2O \tag{1c}$$

$$CH_3NH_3I \rightarrow CH_3NH_2\uparrow + HI\uparrow \tag{1d}$$

$$4HI + O_2 \rightarrow 2I_2\uparrow + 2H_2O \tag{1e}$$

However, with additional moisture and time, especially the dihydrate can decompose into CH_3NH_2, PbI_2, HI, I_2 and H_2O, which is irreversible due to the volatility of many of these products [53]. The degradation process can be slowed down by choosing appropriate charge transport layers [44].

In case when a bilayer ETL of the PCBM/C_{60} is used, not only passivation of the trap states takes place, but also the hysteresis diminishes and the cell humidity stability improves due to the hydrophobic nature of the PCBM top layer in the inverted cell [37]. Another option how to slow down degradation could be making the top electrode thick enough. However, at the present time it is difficult to find data in literature on how the top electrode thickness influences cell degradation during its exposure to ambient air after thermal deposition of the top electrode.

As far as we know, there is only one study in literature, which considers the pressure influence upon the solar cell parameters [62]; yet its authors have investigated only the open-circuit voltage (V_{OC}) change kinetics in vacuum and only for a direct mesoporous pure-triiodide perovskite cell. Similar investigations for the inverted planar mixed halide perovskite $CH_3NH_3PbI_{3-x}Cl_x$ cell, to our knowledge, have not been reported.

Most studies involve only determining the spectral dependence of the short-circuit photocurrent (SCP) EQE (see, for example, [1], [37], [63]), but it is not always possible to reliably describe the cell response to varying external factors by acquiring of just this single parameter. Therefore, additional spectral dependencies for the fill factor (FF), V_{OC} and the power conversion efficiency (PCE) determined before and after the cell exposure to air could be useful to describe the first steps of degradation. We have not found such a type of cell characterisation reported in the literature.

3. CONCLUSION

1. The main physical parameters concerning high change carrier mobility, very low recombination rates, large carrier life time and diffusion length, large absorption coefficients and very weak exciton binding energies have been reported to explain very impressive performance of organic-inorganic perovskite solar cells.

2. Literature analysis has shown that adding a small amount of Cl^- ions in Pb triiodide perovskite (mixed halide perovskite cells) has a favourable effect on the above-mentioned physical parameters.

3. Employing the double electron transport layer (ETL) $PCBM/C_{60}$ is beneficiary because it is clearly evident that such ETL passivates the shallow and also deep trap states and diminishes hysteresis. Double ETL also improves the cell humidity stability by its hydrophobic nature. These observations demonstrate how important is to choose hydrophobic character charge carrier transport layers to diminish the cell degradation processes.

4. To get a deeper insight into organic-inorganic perovskite solar cell degradation processes, it would be valuable to study spectral dependencies of FF and Voc. This could provide valuable information about cell PCE spectral changes under degradation as well as better understanding of what occurs with charge carrier recombination processes and possible hot carrier participation.

ACKNOWLEDGEMENTS

REFERENCES

1. Burschka, J., Pellet, N., Moon, S.-J., Humphry-Baker, R., Gao, P., Nazeeruddin, M. K., & Grätzel, M. (2013). Sequential Deposition as A Route to High-Performance Perovskite-Sensitized Solar Cells. *Nature*, *499* (7458), 316–319. DOI: 10.1038/nature12340

2. Liu, M., Johnston, M. B., & Snaith, H. J. (2013). Efficient Planar Heterojunction Perovskite Solar Cells by Vapour Deposition. *Nature*, *501* (7467), 395–398. DOI: 10.1038/nature12509

3. Cressey, D., Ledford, H., Reardon, S., Gibney, E., Tollefson, J., Schiermeier, Q., & Peplow, M. (2013). 365 Days: Nature's 10. *Nature*, *504* (7480), 357–365. DOI: 10.1038/504357a

4. Zhao, Y., & Zhu, K. (2016). Organic–Inorganic Hybrid Lead Halide Perovskites for Optoelectronic and Electronic Applications. *Chemical Society Reviews*, *45* (3), 655–689. DOI: 10.1039/C4CS00458B

5. Best Research-Cell Efficiency Chart. (2019). *National Renewable Energy Laboratory*. Retrieved 1 August 2019, from https://www.nrel.gov/pv/assets/pdfs/best-research-cell-efficiencies.20190703.pdf

6. Wehrenfennig, C., Eperon, G. E., Johnston, M. B., Snaith, H. J., & Herz, L. M. (2014). High Charge Carrier Mobilities and Lifetimes in Organolead Trihalide Perovskites. *Advanced Materials*, *26* (10), 1584–1589. DOI: 10.1002/adma.201305172

7. Bretschneider, S. A., Weickert, J., Dorman, J. A., & Schmidt-Mende, L. (2014). Research Update: Physical and Electrical Characteristics of Lead Halide Perovskites for Solar Cell Applications. *APL Materials*, *2* (4), 040701. DOI: 10.1063/1.4871795

8. Mei, A., Li, X., Liu, L., Ku, Z., Liu, T., Rong, Y., & Han, H. (2014). A Hole-Conductor-Free, Fully Printable Mesoscopic Perovskite

Solar Cell with High Stability. *Science*, *345* (6194), 295–298. DOI: 10.1126/science. 1254763

9. Yang, W. S., Noh, J. H., Jeon, N. J., Kim, Y. C., Ryu, S., Seo, J., & Seok, S. I. (2015). High-Performance Photovoltaic Perovskite Layers Fabricated through Intramolecular Exchange. *Science*, *348* (6240), 1234–1237. DOI: 10.1126/science.aaa9272

10. Qing, J., Chandran, H.-T., Cheng, Y.-H., Liu, X.-K., Li, H.-W., Tsang, S.-W., & Lee, C.-S. (2015). Chlorine Incorporation for Enhanced Performance of Planar Perovskite Solar Cell Based on Lead Acetate Precursor. *ACS Applied Materials & Interfaces*, *7* (41), 23110–23116. DOI: 10.1021/acsami.5b06819

11. de Quilettes, D. W., Vorpahl, S. M., Stranks, S. D., Nagaoka, H., Eperon, G. E., Ziffer, M. E., & Ginger, D. S. (2015). Impact of Microstructure on Local Carrier Lifetime in Perovskite Solar Cells. *Science*, *348* (6235), 683–686. DOI: 10.1126/science.aaa5333

12. Fan, L., Ding, Y., Luo, J., Shi, B., Yao, X., Wei, C., & Zhang, X. (2017). Elucidating the Role of Chlorine in Perovskite Solar Cells. *Journal of Materials Chemistry A*, *5* (16), 7423–7432. DOI: 10.1039/C7TA00973A

13. Dong, Q., Fang, Y., Shao, Y., Mulligan, P., Qiu, J., Cao, L., & Huang, J. (2015). Electron-Hole Diffusion Lengths > 175 µm in Solution-Grown $CH_3NH_3PbI_3$ Single Crystals. *Science*, *347* (6225), 967–970. DOI: 10.1126/science.aaa5760

14. Stranks, S. D., Eperon, G. E., Grancini, G., Menelaou, C., Alcocer, M. J. P., Leijtens, T., & Snaith, H. J. (2013). Electron-Hole Diffusion Lengths Exceeding 1 Micrometer in an Organometal Trihalide Perovskite Absorber. *Science*, *342* (6156), 341–344. DOI: 10.1126/science.1243982

15. Xing, G., Mathews, N., Sun, S., Lim, S. S., Lam, Y. M., Gratzel, M., & Sum, T. C. (2013). Long-Range Balanced Electron- and Hole-Transport Lengths in Organic-Inorganic $CH_3NH_3PbI_3$. *Science*, *342* (6156), 344–347. DOI: 10.1126/science.1243167

16. Hutter, E. M., Eperon, G. E., Stranks, S. D., & Savenije, T. J. (2015). Charge Carriers in Planar and Meso-Structured Organic–Inorganic Perovskites: Mobilities, Lifetimes, and Concentrations of Trap States. *The Journal of Physical Chemistry Letters*, *6* (15), 3082–3090. DOI: 10.1021/acs.jpclett.5b01361

17. Green, M. A., Ho-Baillie, A., & Snaith, H. J. (2014). The Emergence of Perovskite Solar Cells. *Nature Photonics*, *8* (7), 506–514. DOI: 10.1038/nphoton.2014.134

18. Miyasaka, T. (2015). Perovskite Photovoltaics: Rare Functions of Organo Lead Halide in Solar Cells and Optoelectronic Devices. *Chemistry Letters*, *44* (6), 720–729. DOI: 10.1246/cl.150175

19. Kojima, A., Teshima, K., Shirai, Y., & Miyasaka, T. (2009). Organometal Halide Perovskites as Visible-Light Sensitizers for Photovoltaic Cells. *Journal of the American Chemical Society*, *131* (17), 6050–6051. DOI: 10.1021/ja809598r

20. Colella, S., Mosconi, E., Fedeli, P., Listorti, A., Gazza, F., Orlandi, F., & Mosca, R. (2013). $MAPbI_{3-x}Cl_x$ Mixed Halide Perovskite for Hybrid Solar Cells: The Role of Chloride as Dopant on the Transport and Structural Properties. *Chemistry of Materials*, *25* (22), 4613–4618. DOI: 10.1021/cm402919x

21. Zheng, L., Zhang, D., Ma, Y., Lu, Z., Chen, Z., Wang, S., & Gong, Q. (2015). Morphology Control of the Perovskite Films for Efficient Solar Cells. *Dalton Transactions*, *44* (23), 10582–10593. DOI: 10.1039/C4DT03869J

22. Kaltenbrunner, M., Adam, G., Głowacki, E. D., Drack, M., Schwödiauer, R., Leonat, L., & Bauer, S. (2015). Flexible High Power-Per-Weight Perovskite Solar Cells with Chromium Oxide–Metal Contacts for Improved Stability in Air. *Nature Materials*, *14* (10), 1032–1039. DOI: 10.1038/nmat4388

23. Saba, M., Quochi, F., Mura, A., & Bongiovanni, G. (2016). Excited State Properties of Hybrid Perovskites. *Accounts of Chemical Research*, *49* (1), 166–173. DOI: 10.1021/acs.accounts.5b00445

24. Lin, Q., Armin, A., Nagiri, R. C. R., Burn, P. L., & Meredith, P. (2015). Electro-Optics of Perovskite Solar Cells. *Nature Photonics*, *9* (2), 106–112. DOI: 10.1038/nphoton.2014.284

25. Yamada, Y., Nakamura, T., Endo, M., Wakamiya, A., & Kanemitsu, Y. (2015). Photoelectronic Responses in Solution-Processed Perovskite $CH_3NH_3PbI_3$ Solar Cells Studied by Photoluminescence and Photoabsorption Spectroscopy. *IEEE Journal of Photovoltaics*, *5* (1), 401–405. DOI: 10.1109/JPHOTOV.2014.2364115

26. Miyata, A., Mitioglu, A., Plochocka, P., Portugall, O., Wang, J. T.-W., Stranks, S. D., & Nicholas, R. J. (2015). Direct Measurement of the Exciton Binding Energy and Effective Masses for Charge Carriers in Organic–Inorganic Tri-Halide Perovskites. *Nature Physics*, *11* (7), 582–587. DOI: 10.1038/nphys3357

27. Ruf, F., Aygüler, M. F., Giesbrecht, N., Rendenbach, B., Magin, A., Docampo, P., & Hetterich, M. (2019). Temperature-Dependent Studies of Exciton Binding Energy and Phase-Transition Suppression in (Cs,FA,MA)Pb(I,Br)$_3$ Perovskites. *APL Materials*, *7* (3), 031113. DOI: 10.1063/1.5083792

28. Tombe, S., Adam, G., Heilbrunner, H., Yumusak, C., Apaydin, D. H., Hailegnaw, B., & Scharber, M. C. (2018). The Influence of Perovskite Precursor Composition on the Morphology and Photovoltaic Performance of Mixed Halide $MAPbI_{3-x}Cl_x$ Solar Cells. *Solar Energy*, *163*, 215–223. DOI: 10.1016/j.solener.2018.01.083

29. Yu, H., Wang, F., Xie, F., Li, W., Chen, J., & Zhao, N. (2014). The Role of Chlorine in the Formation Process of "$CH_3NH_3PbI_{3-x}Cl_x$" Perovskite. *Advanced Functional Materials*, *24* (45), 7102–7108. DOI: 10.1002/adfm.201401872

30. Xie, F. X., Su, H., Mao, J., Wong, K. S., & Choy, W. C. H. (2016). Evolution of Diffusion Length and Trap State Induced by Chloride in Perovskite Solar Cell. *The Journal of Physical Chemistry C*, *120* (38), 21248–21253. DOI: 10.1021/acs.jpcc.6b06914

31. Stewart, R. J., Grieco, C., Larsen, A. V., Doucette, G. S., & Asbury, J. B. (2016). Molecular Origins of Defects in Organohalide Perovskites and Their Influence on Charge Carrier Dynamics. *The Journal of Physical Chemistry C*, *120* (23), 12392–12402. DOI: 10.1021/acs.jpcc.6b03472

32. Lee, M. M., Teuscher, J., Miyasaka, T., Murakami, T. N., & Snaith, H. J. (2012). Efficient Hybrid Solar Cells Based on Meso-Superstructured Organometal Halide Perovskites. *Science*, *338* (6107), 643–647. DOI: 10.1126/science.1228604

33. Di Giacomo, F., Zardetto, V., Lucarelli, G., Cinà, L., Di Carlo, A., Creatore, M., & Brown, T. M. (2016). Mesoporous Perovskite Solar Cells and the Role of Nanoscale Compact Layers for Remarkable All-Round High Efficiency under both Indoor and Outdoor Illumination. *Nano Energy*, *30*, 460–469. DOI: 10.1016/j.nanoen.2016.10.030

34. Fan, Y., Qin, H., Ye, W., Liu, M., Huang, F., & Zhong, D. (2018). Improving the Stability of Methylammonium Lead Iodide Perovskite Solar Cells by Cesium Doping. *Thin Solid Films*, *667*, 40–47. DOI: 10.1016/j.tsf.2018.10.001

35. You, J., Hong, Z., Yang, Y. (Michael), Chen, Q., Cai, M., Song, T.-B., & Yang, Y. (2014). Low-Temperature Solution-Processed Perovskite Solar Cells with High Efficiency and Flexibility. *ACS Nano*, *8* (2), 1674–1680. DOI: 10.1021/nn406020d

36. Liang, P.-W., Liao, C.-Y., Chueh, C.-C., Zuo, F., Williams, S. T., Xin, X.-K., & Jen, A. K.-Y. (2014). Additive Enhanced Crystallization of Solution-Processed Perovskite for Highly Efficient Planar-Heterojunction Solar Cells. *Advanced Materials*, *26* (22), 3748–3754. DOI: 10.1002/adma.201400231

37. Heo, J. H., Han, H. J., Kim, D., Ahn, T. K., & Im, S. H. (2015). Hysteresis-Less Inverted $CH_3NH_3PbI_3$ Planar Perovskite Hybrid Solar Cells with 18.1% Power Conversion Efficiency. *Energy & Environmental Science*, *8* (5), 1602–1608. DOI: 10.1039/C5EE00120J

38. Ye, M., Hong, X., Zhang, F., & Liu, X. (2016). Recent Advancements in Perovskite Solar Cells: Flexibility, Stability And Large Scale. *Journal of Materials Chemistry A*, *4* (18), 6755–6771. DOI: 10.1039/C5TA09661H

39. Chen, Y., Chen, T., & Dai, L. (2015). Layer-by-Layer Growth of $CH_3NH_3PbI_{3-x}Cl_x$ for Highly Efficient Planar Heterojunction Perovskite Solar Cells. *Advanced Materials*, *27* (6), 1053–1059. DOI: 10.1002/adma.201404147

40. Seo, J., Park, S., Chan Kim, Y., Jeon, N. J., Noh, J. H., Yoon, S. C., & Seok, S. Il. (2014). Benefits of Very Thin PCBM and LiF Layers for Solution-Processed *p–i–n* Perovskite Solar Cells. *Energy Environ. Sci.*, *7* (8), 2642–2646. DOI: 10.1039/C4EE01216J

41. Lian, J., Wang, Q., Yuan, Y., Shao, Y., & Huang, J. (2015). Organic Solvent Vapor Sensitive Methylammonium Lead Trihalide Film Formation for Efficient Hybrid Perovskite Solar Cells. *Journal of Materials Chemistry A*, *3* (17), 9146–9151. DOI: 10.1039/C5TA01595B

42. Chern, Y.-C., Wu, H.-R., Chen, Y.-C., Zan, H.-W., Meng, H.-F., & Horng, S.-F. (2015). Reliable Solution Processed Planar Perovskite Hybrid Solar Cells with Large-Area Uniformity by Chloroform Soaking and Spin Rinsing Induced Surface Precipitation. *AIP Advances*, *5* (8), 087125. DOI: 10.1063/1.4928516

43. Huang, J., Wang, M., Ding, L., Deng, J., & Yao, X. (2016). Efficiency enhancement of the $MAPbI_{3-x}Cl_x$-Based Perovskite Solar Cell by a Two-Step Annealing Procedure. *Semiconductor Science and Technology*, *31* (2), 025009. DOI: 10.1088/0268-1242/31/2/025009

44. Zhao, P., Kim, B. J., & Jung, H. S. (2018). Passivation in Perovskite Solar Cells: A Review. *Materials Today Energy*, *7*, 267–286. DOI: 10.1016/j.mtener.2018.01.004

45. Yu, Y.-Y., Teng, C.-F., Tseng, C., & Wang, Z.-Q. (2018). Fabrication and Characterization of a Solution-Processed Electron Transport Layer for Organic-Inorganic Hybrid Halide Perovskite Photovoltaics. *Thin Solid Films*, *660*, 789–796. DOI: 10.1016/j.tsf.2018.03.057

46. Yerramilli, A. S., Chen, Y., Knight, A., Gogoi, B., Li, L., Song, Y., & Alford, T. L. (2019). Improved Performance of Inverted Perovskite Solar Cells due to the Incorporation of Zirconium Acetylacetonate Buffer Layer. *Solar Energy Materials and Solar Cells*, *200*, 109927. DOI: 10.1016/j.solmat.2019.109927

47. Bao, X., Wang, Y., Zhu, Q., Wang, N., Zhu, D., Wang, J., & Yang, R. (2015). Efficient Planar Perovskite Solar Cells with Large Fill Factor and Excellent Stability. *Journal of Power Sources*, *297*, 53–58. DOI: 10.1016/j.jpowsour.2015.07.081

48. Shao, Y., Xiao, Z., Bi, C., Yuan, Y., & Huang, J. (2014). Origin and Elimination of Photocurrent Hysteresis by Fullerene Passivation in $CH_3NH_3PbI_3$ Planar Heterojunction Solar Cells. *Nature Communications*, *5* (1), 5784. DOI: 10.1038/ncomms6784

49. Lopez-Varo, P., Jiménez-Tejada, J. A., García-Rosell, M., Ravishankar, S., Garcia-Belmonte, G., Bisquert, J., & Almora, O. (2018). Device Physics of Hybrid Perovskite Solar cells: Theory and Experiment. *Advanced Energy Materials*, *8* (14), 1702772. DOI: 10.1002/aenm.201702772

50. Wang, Q., Shao, Y., Dong, Q., Xiao, Z., Yuan, Y., & Huang, J. (2014). Large Fill-Factor Bilayer Iodine Perovskite Solar Cells Fabricated by a Low-Temperature Solution-Process. *Energy and Environmental Science*, *7* (7), 2359–2365. DOI: 10.1039/C4EE00233D

51. Niu, G., Guo, X., & Wang, L. (2015). Review of Recent Progress in Chemical Stability of Perovskite Solar Cells. *Journal of Materials Chemistry A*, *3* (17), 8970–8980. DOI: 10.1039/C4TA04994B

52. Zhang, L., & Sit, P. H.-L. (2016). Ab Initio Static and Dynamic Study of $CH_3NH_3PbI_3$ Degradation in the Presence of Water, Hydroxyl Radicals, and Hydroxide Ions. *RSC Advances*, *6* (80), 76938–76947. DOI: 10.1039/C6RA12781A

53. Shahbazi, M., & Wang, H. (2016). Progress in Research on the Stability of Organometal Perovskite Solar Cells. *Solar Energy*, *123*, 74–87. DOI: 10.1016/j.solener.2015.11.008

54. Yang, J., & Kelly, T. L. (2017). Decomposition and Cell Failure Mechanisms in Lead Halide Perovskite Solar Cells. *Inorganic Chemistry*, *56* (1), 92–101. DOI: 10.1021/acs.inorgchem.6b01307

55. Asghar, M. I., Zhang, J., Wang, H., & Lund, P. D. (2017). Device Stability of Perovskite Solar Cells – A Review. *Renewable and Sustainable Energy Reviews*, *77*, 131–146. DOI: 10.1016/j.rser.2017.04.003

56. Wang, R., Mujahid, M., Duan, Y., Wang, Z.-K., Xue, J., & Yang, Y. (2019). A Review of Perovskites Solar Cell Stability. *Advanced Functional Materials*, 1808843. DOI: 10.1002/adfm.201808843

57. Wang, D., Wright, M., Elumalai, N. K., & Uddin, A. (2016). Stability of Perovskite Solar Cells. *Solar Energy Materials and Solar Cells*, *147*, 255–275. DOI: 10.1016/j.solmat.2015.12.025

58. Li, Y., Xu, X., Wang, C., Ecker, B., Yang, J., Huang, J., & Gao, Y. (2017). Light-Induced Degradation of $CH_3NH_3PbI_3$ Hybrid Perovskite Thin Film. *The Journal of Physical Chemistry C*, *121* (7), 3904–3910. DOI: 10.1021/acs.jpcc.6b11853

59. Li, Y., Xu, X., Wang, C., Wang, C., Xie, F., Yang, J., & Gao, Y. (2015). Degradation by Exposure of Coevaporated $CH_3NH_3PbI_3$ Thin Films. *The Journal of Physical Chemistry C*, *119* (42), 23996–24002. DOI: 10.1021/acs.jpcc.5b07676

60. Song, Z., Abate, A., Watthage, S. C., Liyanage, G. K., Phillips, A. B., Steiner, U., & Heben, M. J. (2016). Perovskite Solar Cell Stability in Humid Air: Partially Reversible Phase Transitions in the PbI_2-CH_3NH_3I-H_2O System. *Advanced Energy Materials*, *6* (19), 1600846. DOI: 10.1002/aenm.201600846

61. Wang, Q., Chen, B., Liu, Y., Deng, Y., Bai, Y., Dong, Q., & Huang, J. (2017). Scaling Behavior of Moisture-Induced Grain Degradation in Polycrystalline Hybrid Perovskite Thin Films. *Energy & Environmental Science*, *10* (2), 516–522. DOI: 10.1039/C6EE02941H

62. Hall, G. N., Stuckelberger, M., Nietzold, T., Hartman, J., Park, J.-S., Werner, J., & Bertoni, M. I. (2017). The Role of Water in the Reversible Optoelectronic Degradation of Hybrid Perovskites at Low Pressure. *The Journal of Physical Chemistry C*, *121* (46), 25659–25665. DOI: 10.1021/acs.jpcc.7b06402

63. Nie, W., Tsai, H., Asadpour, R., Blancon, J. C., Neukirch, A. J., Gupta, G., & Mohite, A. D. (2015). High-Efficiency Solution-Processed Perovskite Solar Cells with Millimeter-Scale Grains. *Science*, *347* (6221). DOI: 10.1126/science.aaa0472

sciendo

PEROVSKITE CH$_3$NH$_3$PbI$_{3-x}$Cl$_x$ SOLAR CELLS. EXPERIMENTAL STUDY OF INITIAL DEGRADATION KINETICS AND FILL FACTOR SPECTRAL DEPENDENCE

I. Kaulachs[*,1,2], A. Ivanova[2,3], A. Holsts[4], M. Roze[3], A. Flerov[5],
A. Tokmakov[1], I. Mihailovs[1,3], M. Rutkis[1]

[1] Institute of Solid State Physics, University of Latvia,
8 Ķengaraga Str., Riga, LV-1063, LATVIA
[2] Institute of Physical Energetics,
11 Krīvu Str., Riga, LV-1006, LATVIA
[3] Institute of Applied Chemistry, Riga Technical University,
3 Paula Valdena Str., Riga, LV-1048, LATVIA
[4] Ltd Energolukss,
46/2 Ulbrokas Str, Riga, LV-1021, LATVIA
[5] Institute of Physics, University of Latvia,
32 Miera Str., Salaspils, LV-2169, LATVIA
* e-mail: igors.kaulacs@cfi.lu.lv

The main drawback of the methylammonium lead halide perovskite solar cells is their degradation in ambient atmosphere. To investigate ambient-air-induced cell degradation, spectral dependencies of open-circuit voltage (V_{OC}), fill factor (FF) and the power conversion efficiency (PCE) have been acquired (for the first time reported in literature).

Our custom-made measurement system allowed us to perform measurements of the above-mentioned entities *in situ* directly in vacuum during and after thermal deposition of the electrode. We also studied how these parameters in vacuum changed after cell exposure to ambient air for 85 min (50 nm top electrode) and for 180 min (100 nm top Ag electrode). For fresh CH$_3$NH$_3$PbI$_{3-x}$Cl$_x$ cell (never been in open air) with very high shunt resistance of $3 \cdot 10^7$ Ω·cm^2 (with practically no shorts and therefore FF could be determined mainly by charge carrier recombination processes) we found that FF in vacuum increased along with an increase of the incident photon energy from 0.55 at 760 nm up to 0.82 at 400 nm. Hypothesis considering hot

polaron participation in charge carrier photogeneration and recombination processes as well as another competing hypothesis were offered as possible explanations for the observed FF increase.

The kinetics of short-circuit photocurrent EQE with a change in pressure was also investigated. It was also shown that perovskite solar cell degradation could be noticeably reduced by increasing the top Ag electrode thickness to at least 100 nm, which could possibly facilitate the usual encapsulation process.

Keywords: *Degradation kinetics, fill factor spectral dependence, lead halide perovskite, power conversion efficiency, solar cells.*

1. INTRODUCTION

In the previous short literature review, we described the advantages of a low-temperature-developed inverted perovskite solar cell ITO/PEDOT:PSS/$CH_3NH_3PbI_{3-x}$ Cl_x/$PC_{60}BM$/C_{60}/Ag and mentioned that the main drawback of it was degradation in ambient atmosphere [1]. Despite numerous reports existing about perovskite solar cell degradation during long periods of time such as days or months in ambient atmosphere, we did not find any report considering the degradation within short periods of time immediately after the deposition of the top electrode and the following vacuum change in the measurement chamber. Therefore, we developed a cell production and measuring system which allowed us to investigate kinetics of the first stage of degradation *in situ*, not only immediately after the top electrode deposition but also during the following decrease in vacuum up to the ambient atmospheric pressure and pumping back to the high vacuum (~$5 \cdot 10^{-7}$ torr). Thus, we present here the change kinetics of the short-circuit photocurrent (SCP) external quantum efficiency (EQE) during the slow decrease of the vacuum up to the ambient atmosphere conditions – as far as we know, for the first time in literature for such cells.

We found that an increase in the thickness of the top Ag electrode from 50 nm to 100 nm noticeably decreased the speed of cell degradation in the open air.

Spectral dependencies of other photovoltaic parameters such as open-circuit voltage (V_{OC}), power conversion efficiency (PCE) and fill factor (FF) were also acquired in the spectral range of 380–780 nm. Those measurements of spectral dependences are necessary for calculating spectral dependence of PCE, which may be a valuable parameter for solar cells if we need to use them for illumination that differ from full solar spectrum or if we want to enforce their parameters in some desirable spectral region by creating tandem sells. Those dependences can be used for "hunting" hot charge carrier presence in the cell. It is known than hot carriers in organic-inorganic perovskites give very long lifetime up to 100 ps and so they can appear in solar cells if one manages to receive them on electrodes. For the fresh cells with high shunt resistances of ~$2 \cdot 10^7 \, \Omega \cdot cm^2$, we observed a FF increase from 0.55 at 760 nm up to 0.82 at 400 nm, also for the first time reported in literature. Hypotheses to explain this phenomenon are offered in the present study.
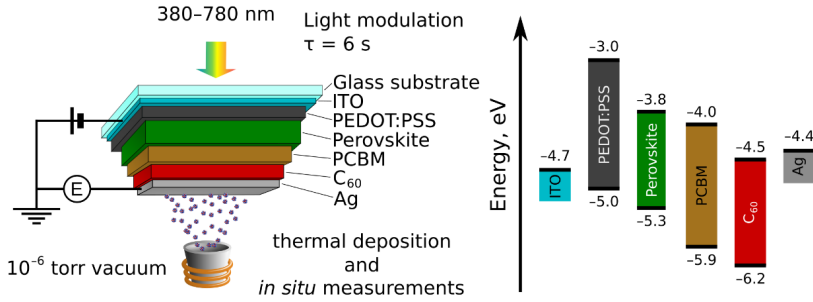
2. EXPERIMENTAL

Fig. 1. The scheme of the experiment and the structure of the studied cells. The layers are sequentially deposited onto the bottom side, while the light is being shined from the top side.

The inverted planar mixed halide perovskite solar cells were fabricated with the following layer configuration: glass/ $ITO/PEDOT:PSS/CH_3NH_3PbI_{3-x}Cl_x/$ $PC_{61}BM/C_{60}/Ag$, using spin-coating from the solutions in the ambient atmosphere and, for the C_{60} and Ag electrode, by thermal vacuum evaporation – as reported previously [2]. The device structure, the energy level diagram of layers and the scheme of the experimental arrangement for *in situ* measurements are shown in Fig. 1.

2.1. Device Preparation: The Wet Part

Patterned ITO substrates (*PGO* 15 ohm/sq) were sequentially cleaned with chloroform, acetone, deionized (DI) water and isopropanol for 15 min each in an ultrasonic bath. After every sonication, the substrates were dump-rinsed in DI water. Poly(3,4-ethylenedioxythiophene) poly(styrenesulfonate) (PEDOT:PSS, *Clevios Baytron AI4083*) was deposited by spin-coating at 6500 rpm, at acceleration of 3000 rpm/s for 60 sec and annealed at 145 °C for 1 hour in the argon atmosphere. Then the perovskite absorber $CH_3NH_3PbI_{3-x}Cl_x$ was deposited by a modified interdiffusion method [3]: the mixture of PbI_2 (*Sigma Aldrich*, 99.999 % purity with trace metal bases) and $PbCl_2$ (*Sigma Aldrich*, 99.999 % purity with trace metal bases) with a molar ratio 3.4:1 was dissolved in the mixture of *N,N*-dimethylformamide (DMF; *Sigma Aldrich*, 99.8 %) and dimethylsulfoxide (DMSO; *Sigma Aldrich*, 99.9 %) with a molar ratio 3:1 [4], then spin-coated in the ambient air at a rate of 6500 rpm and acceleration of 3000 rpm/s at 65 °C for 75 s, using ~70 µL of 65 °C hot solution. The $PbI_2:PbCl_2$ film was dried as-fabricated for 20 minutes at the room temperature (rt) and for 20 minutes at 70 °C with an aim to remove the remaining solvents and to promote crystallization of the film. Then the cell was placed back on the hot spin-coater at 65 °C, after which ~90 µL of the hot 40 mg/mL methylammonium iodide (MAI; *Sigma Aldrich*, 99.9 %) solution in 2-propanol (IPA; *Sigma Aldrich*, 99.9 %) was squirted onto the middle of the cell, and after ~10 seconds the coating process was started at a speed of 6000 rpm with an acceleration of 3000 rpm/s and continued for 75 s.

Subsequently, the sample was put into

the thermostat at 50 °C, after which the temperature was slowly lifted up to 105 °C at a speed of 1.5 degree per minute. Annealing was continued for 1 h in the ambient air and then for 1 h in the argon atmosphere to finish the interdiffusion process; then the temperature was slowly decreased to the rt. Then the cell was covered with the $PC_{61}BM$ (*American Dye Source*, 99.5 %) layer from a 30 mg/mL solution in 1,2-dichlorobenzene (DCB; *Sigma Aldrich*, 99 %) by spin-coating at the speed of 2000 rpm and acceleration of 800 rpm/s, at the room temperature for 60 sec, using 50 µL of the solution. To improve the interdiffusion efficiency of the $PC_{61}BM$ into the perovskite along the grain boundaries and to remove the remaining solvents, the cell was again annealed for 1 hour in the argon atmosphere at 100 °C, slowly rising the temperature from 50 °C to 100 °C and then slowly lowering back to 50 °C.

2.2. Device Preparation: The Vacuum Part

Then an absorption spectrum of the cell was obtained, after which it was transferred to the custom-made vacuum system where about a 40 nm–thick C_{60} layer and an Ag electrode were thermally deposited in the vacuum of 10^{-6} torr. The photoelectric measurements were then performed *in situ*, without any moving of the cell. The double fullerene layer was used to passivate the deep and the shallow trap states [5]–[7]. The active cell area was 7 mm^2 according to the top electrode area. During the deposition of the top Ag electrode, the ohmic resistance and thickness of the electrode as well as the short-circuit current EQE were simultaneously measured while illuminating the cell via the bottom PEDOT:PSS electrode through the quartz window of the vacuum chamber by monochromatic light of 720 nm with an intensity of 10^{15} phot/(cm^2·s). Such a low quanta energy was used to avoid any possible photochemical processes in the cell.

Thus, the minimal thickness of the Ag electrode was chosen to be 50 nm, at which the value of the short-circuit photocurrent EQE reached its saturation while increasing the electrode thickness (as it will be shown further in the article, this thickness was enough to perform all the photoelectric measurements in vacuum but too low to protect the cell against fast degradation in the ambient air). The deposition speed and thickness of the thermally evaporated layers were checked by a calibrated 10 MHz quartz oscillator, frequency meter and computer-controlled shutter. The deposition speed for C_{60} was 6.5 Å/s at cell (sample) t = 25 °C. Before the deposition of the Ag electrode, the cell was cooled down a little to t = 13 °C to avoid a possible short-circuit, and the deposition speed was changed from 2 Å/s in the beginning up to 4.5 Å/s at the end of deposition for the 50 nm (thin) layer and to 7 Å/s for the 100 nm (thick) Ag.

2.3. In Situ Measurements

The cells were illuminated via the ITO electrode (see Fig. 1) by a chopper-modulated monochromatic light in the 370÷900 nm spectral region with an intensity of $10^9÷10^{15}$ phot/(cm^2·s), coming from a 250 W high-pressure xenon lamp through a grating monochromator. Appropriate filters were used to eliminate the second-order effects and the stray light. The selected light modulation period was chosen to be 6 s long, and the intensity was controlled by a calibrated Si photodiode. A constant photon flux onto our cell during the measurement of the spectral and the current–voltage

dependencies was achieved by computer-controlled movements of a *Thorlabs* linear variable ND metallic optical filter with the correction against the Si photodiode spectral sensitivity [8].

Synchrodetection technique [9] with the use of PC-controlled data storage, evaluating the mean value and the root-mean-square deviation (RMSD) allowed achieving the measurement accuracy of 1.5 %. The current (EQE)–voltage dependence measurements were made with a step of 0.05 V, the time for a single step varying from multiple minutes to 2 hours (depending on the level of the current noise) to ensure the aforementioned accuracy level of 1.5 % at the high-voltage end. After setting the next voltage value, a 20-second dead time was introduced to avoid the influence of transition processes. Hence, our EQE–voltage curves can be considered as if static. The magnitude of the dark current was permanently monitored by taking the endpoint value of the residual current during each dark half-period of the light modulation.

During the time-and-pressure-dependent SCP EQE evolution experiment, measurements were checked every 30–1000 light–dark periods, the light being adjusted to 10^{15} phot/(cm²·s) with a relative error (the normalized root-mean-square deviation, NRMSD, calculated as the ratio of the RMSD to the mean value over the aforementioned 30–1000 periods) ± 1 %; for each period the mean value and the NRMSD of the EQE, the light intensity and the value of the photocurrent were collected. This made it possible to achieve the values of the NRMSD of the EQE from ~0.1 % to 0.4 %, and the measurement time of 2 to 55 minutes for each data point stored.

The ambient air that was let in during the experiment had the following properties: 760 torr pressure, ~40 % relative humidity and ~22 °C temperature.

As noted before, the formation of perovskite degradation features of multiple volatile products [10]–[13] should be intensified under vacuum conditions. However, we checked this idea for a cell with 50 nm thin top electrode for two weeks in vacuum and observed a modest (~5 %) decrease in the short-circuit photocurrent EQE at 480 nm, whereas for the 620–720 nm region even a small increase in EQE was observed. Similarly, only minor changes in the properties were observed for the 100 nm thick top electrode cell after 2 months in vacuum.

3. RESULTS AND DISCUSSION

3.1. Cell with 50 nm (Thin) Ag Electrode

Figure 2 shows the dynamics of vacuum influence on the short-circuit photocurrent EQE for the inverted planar mixed-halide perovskite solar cell $CH_3NH_3PbI_{3-x}Cl_x$ by changing pressure in the measurement chamber from $3 \cdot 10^{-7}$ torr to the ambient air conditions (760 torr, ~40 % relative humidity, ~22 °C) and back to 10^{-6} torr for a 26-hour measurement period.

After shutting both the high- and low-vacuum valves, the vacuum slowly dropped from $3 \cdot 10^{-7}$ torr to ~10^{-4} torr over 45 minutes. During this period, the value of the EQE did not change noticeably; however, 45 minutes later the EQE began to increase from 38.3 % to 43.2 %, which continued for 20 minutes (at this moment, 65 minutes had passed since the vacuum pumping was switched off). This peak value (~12 % higher than in high vacuum) remained for

~20 minutes (peak P in Fig. 2); then the EQE began to diminish, reaching its initial high-vacuum value after 2 hours, at which point the pressure in the measurement chamber dropped to 10^{-3} torr. A similar initial increase in the EQE for a direct mesoporous MAPbI3 perovskite solar cell was observed by Z. Song et al. [11]; this initial increase of the short-circui current EQE

for the first $10 \div 20$ minutes was explained by passivation of the surface trap states by the water molecules [14] and the improving contacts between the perovskite crystallites [15]. Song et al., however, carried out their measurements at a relative humidity (RH) of 55 % and 80 % at 1 atmosphere of the N_2 gas; we observed a similar effect.
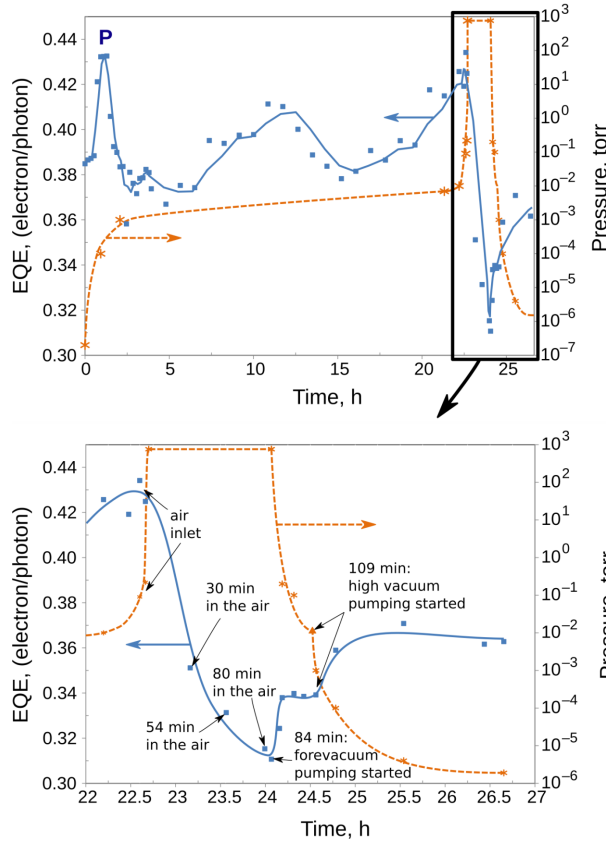

Fig. 2. Time dependence of the pressure change influence on the short-circuit EQE for the ITO/PEDOT:PSS/ $CH_3NH_3PbI_{3-x}Cl_x/PC_{61}BM/C_{60}/Ag$ cell with a 50 nm thick Ag electrode for 720 nm illumination with an intensity of 10^{15} phot/(cm²·s). The curve within the top pane is based on moving average with a period of 5.

By decreasing vacuum from $3 \cdot 10^{-7}$ torr to $\sim 10^{-4}$–10^{-3} torr, the water vapour content in the chamber was lower by many orders of magnitude. Yet in our cell the Ag electrode was very thin (50 nm) and possibly very porous and, hence, easily penetrable by both H_2O and O_2; whereas Song et al. [11] used a dense and continuous gold electrode, relatively impenetrable to water. The water in our case could have originated in the gas phase by continuous desorption from the inner surface of the metallic walls of the measurement chamber and possibly by small leaks in the vacuum chamber (even a small concentration of water could lead to significant changes in the cell [14], [15]).

Here we must mention that by increasing the Ag electrode thickness to 100 nm, as well as its density, by faster evaporation (up to 7.5 Å/sec), this phenomenon was not so expressed anymore.

Then the system was left at slowly changing pressure for the time monitoring of the SCP EQE over ca. 20 h; the pressure slowly increased from 10^{-3} torr to 10^{-2} torr due to non-absolute hermeticity of the chamber. During this time, SCP EQE oscillated with a period of ~10 hours (see Fig. 2), characterizing the complicated diffusion processes of H_2O and O_2 into the cell through different layers and simultaneous back-diffusion of the perovskite destruction products out of the cell. After ~22-hour observation of the cell SCP EQE changes in the forevacuum, the ambient atmosphere (760 torr, 22 °C, RH ~ 40 %) was let into the measurement chamber, initially slowly by slightly opening the valve until the pressure reached $2 \cdot 10^{-1}$ torr (SCP EQE oscillations continued) and then by promptly opening the valve, at which point we observed a fast plunge of the photocurrent EQE from 43 % to 31 % during 85 minutes in the air (Fig. 2). However, as the vacuum pumping was restarted again, the SCP EQE increased back: first, during the period of ~15 minutes in the forevacuum of 10^{-1} torr, to 34 % and saturated at this value; second, when the high-vacuum pumping was started, to ~36–38 %. In addition, the spectral dependence of the SCP EQE remained practically unchanged after pumping back to $5 \cdot 10^{-7}$ torr (see Fig. 3; this pressure was achieved next day after the measurement depicted in Fig. 2 ended).

Here we see that the obtained EQE values are too moderate as it was also previously observed for the cells created by the interdiffusion method on the PEDOT:PSS HTL [16], possibly due to incomplete conversion of the PbI_2:$PbCl_2$ layer to perovskite after the deposition of the MAI layer and the following annealing of the cell. Such a situation is indeed sometimes observed when using a two-step interdiffusion method [16]–[18] where the excessive PbI_2 acts as an insulating layer, reducing the photocurrent [19]. This explanation is also supported by the very high values for shunt resistance (~$3 \cdot 10^7$ $\Omega \cdot cm^2$) and series resistance (R_{ser}; ~ $50 \div 60$ $\Omega \cdot cm^2$) obtained for our cells (see Table 2).
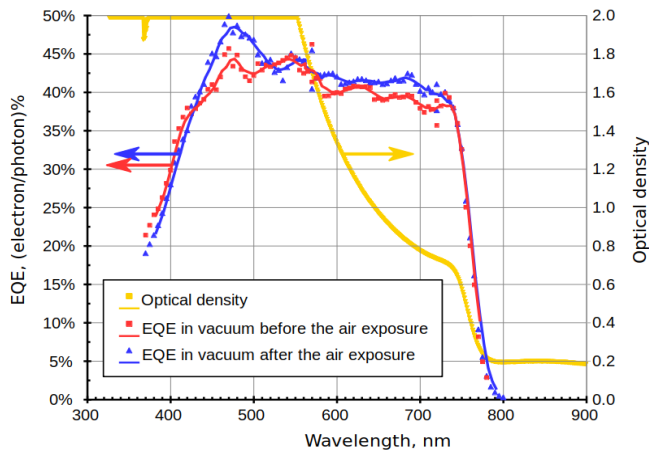

Fig. 3. Spectral dependences of the short-circuit photocurrent (SCP) EQE and the optical density of the perovskite and the PCBM layers for the cell with a 50 nm thick Ag electrode, before and after the exposure to air for 85 min. The curves are smoothed by moving average with a period of 5.

Table 1. The Change in the Electric Properties of the ITO/PEDOT:PSS/CH3NH3PbI3-xClx/PC61BM/C60 / Ag Cell with a 50 nm Thick Ag Electrode after the Air Inlet for 85 Minutes and Subsequent Pumping Back to Vacuum. The values given are the mean values with respect to the different directions of the applied voltage.

λ, nm	EQE, %		FF		V_{OC}, V		PCE, %	
	before	after	before	after	before	after	before	after
480	42	49	0.73	0.29	0.87	1.19	9.8	6.6
720	38	41	0.55	0.26	0.83	1.09	9.7	6.7

Table 2. The Change in the Electric Properties of the Cell With a 50 nm Thick Ag Electrode after the Air Inlet for 85 Minutes and Subsequent Pumping Back to Vacuum (average with respect to different directions of applied voltage).

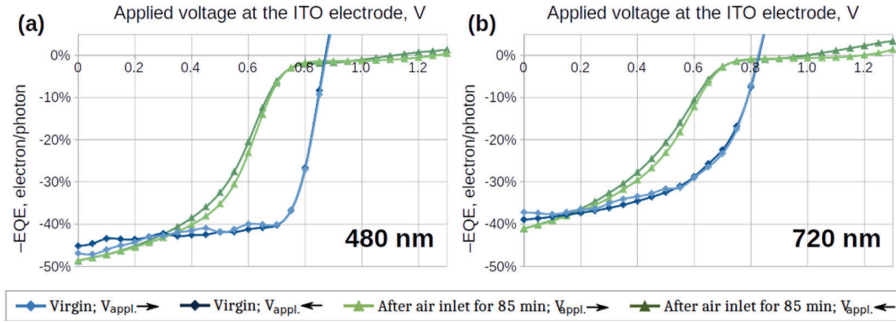| λ, nm	R_{shunt}, Ω·cm²		R_{series}, Ω·cm²	
	before	after	before	after
480	$2.7 \cdot 10^7$	$2.3 \cdot 10^7$	47	640
720	$3.6 \cdot 10^7$	$2.4 \cdot 10^7$	52	670

Fig. 4. The photocurrent EQE dependences on the externally ap¬plied voltage at '+' polarity of the ITO electrode for the light intensity of 10^{15} phot/(cm²·s) and (a) 480 nm or (b) 720 nm wavelength, measured in the vacuum of $5 \cdot 10^{-7}$ torr, for the sample with a 50 nm thick Ag electrode. The lighter curves stand for increasing voltage, the darker ones – for decreasing it; the EQE values are plotted with a negative sign, which indicates the electron flow direction towards the top Ag electrode.

Although the short-circuit photocur-rent EQE in the vacuum did not change significantly after the exposure of the cell to the ambient air (as seen in Fig. 3), the EQE dependence on the applied voltage experienced dramatic changes after the air inlet for 85 minutes and subsequent pump-ing back to $5 \cdot 10^{-7}$ torr, when V_{OC} increased from 0.83 V to 1.1 V (for illumination with 720 nm) and from 0.87 V to 1.2 V (for illumination with 480 nm) – as shown both in Figs. 4 and 5 as well as in Table 1. At the same time, the fill factor (FF) decreased profoundly from 0.78 to 0.30 for 480 nm

and from 0.55 to 0.26 for 720 nm, as seen in Table 1 and Fig. 6; see also Fig. 4.

After the cell exposure to the ambient air for 85 minutes, we observed that the shape of the current–voltage (CV) depen-dence on the cell noticeably changed (Fig. 4) and two distinct regions emerged. The dominant region (represented by dashed lines in Fig. 5) has now [extrapolated] V_{OC} values around ~0.60÷0.70 V, which are less than the values for the freshly made cell (0.83÷0.87 V). The FF corresponding to this dominant region is also lower after the cell exposure to the ambient air than it

was before the air inlet (see Fig. 6). One can conclude that, while the cell had stayed for 85 minutes in the ambient air, new charge-carrier recombination centers were irreversibly created in the cell, intensifying the recombination processes and thus leading to a decrease in both the fill factor and the V_{OC} for the dominant region.
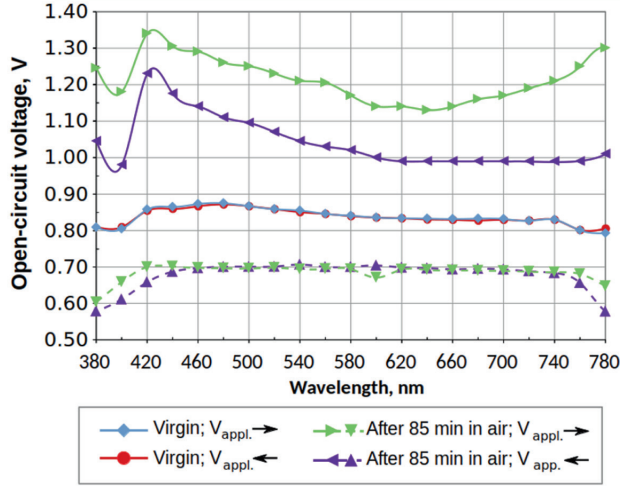

Fig. 5. Spectral dependences of the open-circuit voltage V_{OC}, measured in the vacuum of $5 \cdot 10^{-7}$ torr before and after the air inlet, for the sample with a 50 nm thick Ag electrode. The lighter curves stand for increasing voltage, the darker ones – for decreasing it; the dashed curves characterise the dominant region of the CV dependence plot.
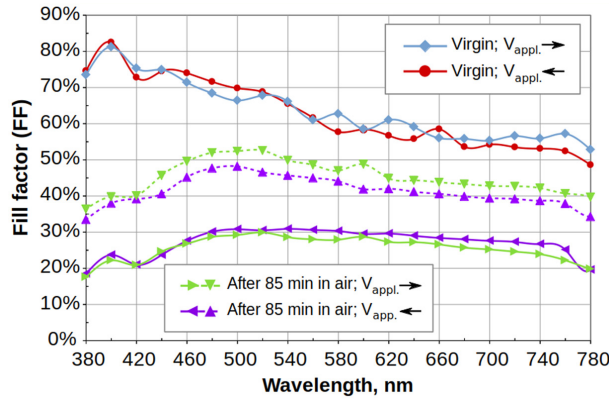

Fig. 6. Spectral dependences of the fill factor, measured in the vacuum of $5 \cdot 10^{-7}$ torr before and after the air inlet, for the sample with a 50 nm thick Ag electrode. The lighter curves stand for increasing voltage, the darker ones – for decreasing it; the finely dashed curves characterise the dominant region of the CV dependence plot.

Apart from the dominant region of the current–voltage characteristic, Fig. 4 also demonstrates a thin long tail over which the V_{OC} increases up to 1.2 V (at 480 nm) – and even higher for shorter wavelengths (Fig. 5). It indicates that after the air inlet into the measurement chamber not only charge recombination centers were cre-

ated but also some fraction of perovskite possibly degraded irreversibly to PbI_2. As it is known such degradation increases the bandgap up to 2.36 eV [10]. Barrier formation for the electron current at the contact of the perovskite layer with the Ag electrode after the air inlet cannot be ruled out, as the series resistance of the cell after the air inlet increased from $50 \div 60$ $\Omega \cdot cm^2$ to more than 600 $\Omega \cdot cm^2$ (details in Table 2).

For this high-voltage tail of Fig. 4, a large hysteresis in the V_{OC} was observed with respect to the direction of the voltage change, as seen in Fig. 5. It indicates the appearance of a large number of the charge-carrier trapping centers after the air inlet. Possibly, these trapping centers intensify the recombination of the photogenerated charge carriers, consequently reducing the fill factor from $0.50 \div 0.82$ for the cell that has only been in the vacuum to ~0.30 after the air was let in and then pumped back out to the high vacuum (as seen in Fig. 6).

For a virgin cell in the vacuum we found an interesting phenomenon: when increasing the energy of the light quanta of the excitation beam, the fill factor increased from 0.50 at 780 nm up to 0.82 at 400 nm, with a relatively steeper increase for the wavelengths shorter than ~600 nm (Fig. 6). The V_{OC} also experienced a mild increase along with an increase in the light quanta energy, as seen in Fig. 5. As far as we know, such a spectral dependence of the fill factor for a metal-organic perovskite solar cell has not been observed before.

At present, we cannot offer a convincing explanation of these phenomena but only propose some hypotheses discussing the hot polarons and their quasi-ballistic transport. It is known that at the room temperature after the photoexcitation, there are very long–lived hot charge carriers in the methyl ammonium lead halide perovskites. The lifetimes of such charge carriers are up to 100 ps [20]–[26], which is about two to three orders of magnitude longer than in the conventional semiconductors [25]. For the large charge-carrier densities (more than 10^{18} cm^{-3}), this is explained by the "hot phonon bottleneck", which originates from the reheating of the charge carriers due to the reabsorption of the phonons [20], [21], [24]. For much lower charge carrier densities of $\leq 10^{16}$ cm^{-3}, which occur under the solar flux and also in the experiments described in the present study, the long-living hot charge carriers can exist due to the formation of spatially large polarons determined by the fast motion of the methylammonium cation as well as the slower motions of the lead halide framework [22]. The reason for these outstandingly large lifetimes of the hot charge carriers is slow cooling of hot polarons by scattering on the acoustic phonons [25], and also by very low thermal conductivity of halide perovskites resulting from short phonon lifetimes [26].

The more the energy of exciting light quanta surpasses the bandgap, the hotter polarons are formed, with increasingly higher both the kinetic energy and the cooling time. Thus, for an excitation energy of 3.14 eV (1.49 eV above the bandgap) in $CH_3NH_3PbI_3$, a quasi-ballistic transport of the hot carriers is observed over up to 230 nm distance and a non-equilibrium transport over up to 600 nm in 100 ps after the excitation, as visualized by the ultrafast microscopy [25]. For lower excitation energy of 1.97 eV (0.32 eV above the band edge), on the other hand, only very little quasi-ballistic transport was detected [25]. Similarly, for the $CH_3NH_3PbI_{3-x}Cl_x$ perovskite (similar to the one in the present investigation) hot charge carriers with the lifetime above 100 ps were observed for the pump photon energies of 3.1 eV and 2.6 eV but were not observed for lower pump energies of 2.05 eV in 100 ps after the excitation [24].

During the quasi-ballistic transport, the charge carriers interact weakly with the trapping centers [24], [25]; therefore, few of them undergo recombination during the transport through the perovskite layer. This can explain the observed increase of the fill factor (which depends directly on the charge carrier recombination) when increasing the photon energy above ~ 2.07 eV (600 nm), as shown in Fig. 6: the higher energy the charge carrier possesses, the longer the distance it travels quasi-ballistically. If it were possible to collect most of these charge carriers at the electrodes, we would observe a strong increase in the V_{OC} value when increasing the incident photon energy above 2.07 eV – but only a small increase from 0.83 eV to 0.87 eV was detected (see Fig. 5), probably because there were substantial losses of the kinetic energy of the hot charge carriers both at the interfaces and inside the charge transport layers, possibly including the insulating layer of PbI_2:$PbCl_2$ (in front of the PEDOT:PSS layer), which remained unconverted from the interdiffusion process when the cell was created.

Fig. 7. Spectral dependences of the power conversion efficiency (PCE), measured in the vacuum of $5 \cdot 10^{-7}$ torr before and after the air inlet for 85 min, for the sample with a 50 nm thick Ag electrode. The lighter curves stand for increasing voltage, the darker ones – for decreasing it.
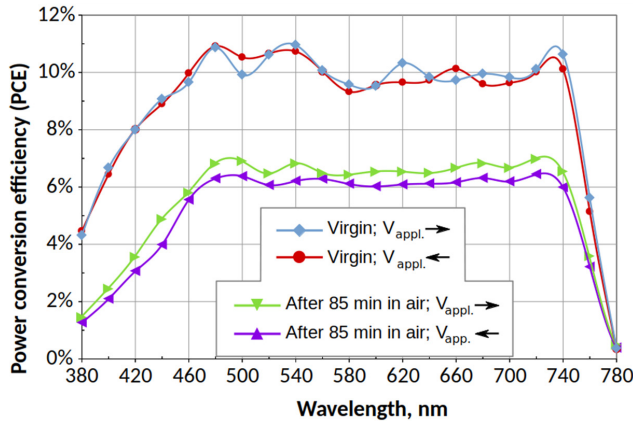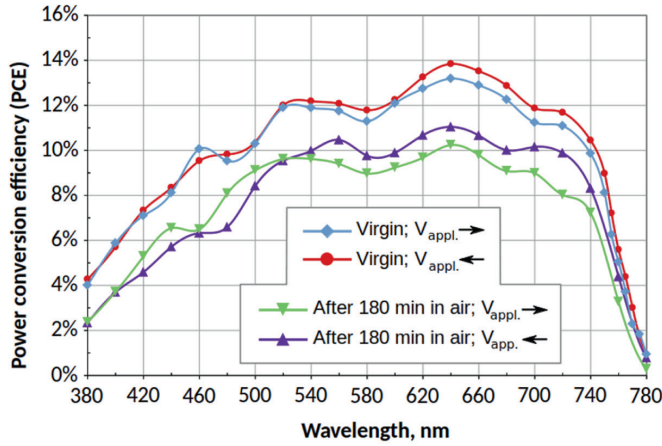

Fig. 8. Spectral dependences of the power conversion efficiency (PCE), measured in the vacuum of $5 \cdot 10^{-7}$ torr before and after the air inlet for 180 min, for the sample with a 100 nm thick Ag electrode. The lighter curves stand for increasing voltage, the darker ones – for decreasing it.

After the cell was exposed to the ambient air for 85 minutes, there was no increase in the FF when moving to the wavelengths of the excitation light shorter than 600 nm anymore (Fig. 6). This could be explained by accumulation of the perovskite degradation product PbI_2, which strongly increased the cooling rate of the hot carriers (observed for the cells produced using a two-step method [20]), and, possibly, by the contact degradation of the Ag electrode, marked by an increase in series resistance of the cell from ~ 50 $\Omega \cdot cm^2$ to more than 600 $\Omega \cdot cm^2$ (Table 2).

Nevertheless, the observed phenomena can also be explained by another hypothesis: when a cell accommodating a large number of the charge carrier traps absorbs light and if the photon energy exceeds the depth of a filled trap plus the applied (external) voltage multiplied by the electron charge, the charge carriers can now go in the opposite direction to the applied external voltage due to energetic considerations. This direction coincides with the flow direction of the charge carriers in the absence of the applied external field. The higher the energy of the photon, the more excess energy is received by the charge carrier released from a trap, and hence the easier it can overcome the applied external field. This, in turn, produces higher opposite-direction extra current, which changes the shape of the photocurrent EQE dependence on the applied voltage in the region of high voltages. Consequently, the observed fill factor should be larger, as is actually seen in Fig. 6 (compare also the curves for the virgin cell in Figs. 4a and 4b). Such a situation is possible when the local electric field in the cell is strongly non-uniform and when some processes of trap filling from external sources take place. Such a process can be the dark injection from the electrodes. Still, this is only a hypothesis, and at present we have no exact explanation for an increase in the FF when increasing the incident photon energy.

Using the obtained spectral dependences for the EQE, the FF and the V_{OC}, we can construct spectral dependences for the power conversion efficiency (PCE) using the following formula [8]:

$$PCE = \frac{V_{OC} \cdot FF \cdot EQE}{E_{phot}}, \qquad (1)$$

where V_{OC} – the open-circuit voltage, V;
FF – the fill factor;
EQE – the external quantum efficiency for the short-circuit photocurrent;
E_{phot} – the incident photon energy, eV.

The PCE spectral dependences for the cell with a 50 nm thin electrode are shown in Fig. 7. This quantity is rather constant within the range of 480–740 nm, despite the fact that the optical density of the sample varies significantly between 550 and 740 nm. One reason is the Ag top electrode (not present when the absorption spectrum was acquired) acting as a mirror for the light to pass multiple times in the sample, thus facilitating more complete absorption. It can also be seen that after the exposure to the ambient air, the PCE decreased 1.5 times at 720 nm, and even more at wavelengths shorter than 460 nm. At 400 nm, this decrease in the PCE even approached 3 times. This is mainly due to a dramatic decrease in the fill factor, as seen in Table 1 and Fig. 6. Much lesser degradation of the cell performance under the exposure to the ambient air was observed for the cell with increased thickness of the top Ag electrode (100 nm instead of 50 nm). This will be discussed in the following section of the article.

3.2. Cell with 100 nm (Thick) Ag Electrode

The spectral dependences of the PCE for the cell with a 100 nm thick Ag electrode are shown in Fig. 8. This cell experienced a twice as long (180 min) exposure to the ambient atmosphere in the measurement chamber compared to the one with a thin electrode; nevertheless, as can be seen in Fig. 8, the PCE suffered much lesser reduction for this cell (compare Figs. 8 and 7). Here we must admit that both cells are not absolutely identical because the one with a thick electrode shows lower PCE values in the short-wavelength region, possibly indicating a thicker layer of the leftover PbI2:PbCl2 left unconverted during cell fabrication. In addition, the shunt resistance for the thick-electrode cell is about an order of magnitude lower than for the thin-electrode cell – this is probably evidence of higher pinhole concentration. Yet we hope that these differences do not obstruct the comparison of the Ag electrode protecting properties in both cases: the diminution of the PCE for the cell with a 100 nm thick electrode is only 1.2 times at 720 nm and 1.6 times at 400 nm (Fig. 8 and Table 3) while for the cell with a 50 nm thick electrode, exposed to the ambient air for half as long, it was 1.5 times at 720 nm and ~3 times at 400 nm. The series resistance for the cell with a thicker Ag electrode increased from 30÷35 $\Omega \cdot cm^2$ to 50÷60 $\Omega \cdot cm^2$ after a 180 min exposure (see Table 4) while for the cell with a thinner electrode the increase was much stronger, from ~50 $\Omega \cdot cm^2$ to 640÷670 $\Omega \cdot cm^2$, for only 85 min exposure (see Table 2). The decrease in the fill factor after the exposure to the ambient air was also much smaller for the cell with 100 nm thick top Ag electrode than for the cell with 50 nm thick Ag electrode (compare Table 3 with Table 1). We can conclude that the increase in the top Ag electrode thickness just by 50 nm (from 50 nm to 100 nm) significantly improves the protection of the cell from the ambient atmosphere influence. Therefore, it becomes possible to perform subsequent encapsulation under ambient conditions instead of the glovebox.

Table 3. The Change in the Electric Properties of the ITO/PEDOT:PSS/CH₃NH₃PbI₃₋ₓClₓ/PC₆₁BM/C₆₀/Ag Cell with a 100 nm Thick Ag Electrode after the Air Inlet for 180 Minutes and Subsequent Pumping Back to Vacuum. The values given are the mean values with respect to the different directions of the applied voltage.

λ, nm	EQE, %		FF		V_{oc}, V		PCE, %	
	before	after	before	after	before	after	before	after
480	45	36	0.64	0.52	0.88	0.92	9.7	6.4
720	39	39	0.60	0.51	0.83	0.85	11	9.6

Table 4. The Change in the Electric Properties of the Cell with a 100 nm Thick Ag Electrode after the Air Inlet for 180 Minutes and Subsequent Pumping Back to Vacuum (average with respect to different directions of applied voltage)

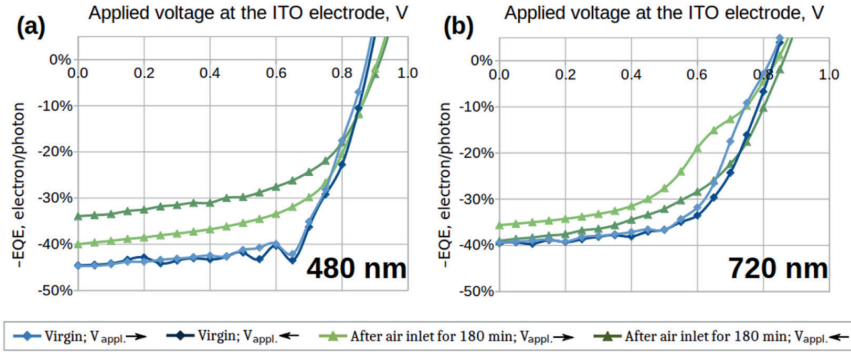| λ, nm	R_{shunt}, $\Omega \cdot cm^2$		R_{series}, $\Omega \cdot cm^2$	
	before	after	before	after
480	$3.1 \cdot 10^6$	$2.0 \cdot 10^6$	35	64
720	$3.9 \cdot 10^6$	$2.2 \cdot 10^6$	31	52

Fig. 9. The photocurrent EQE dependences on the externally applied voltage at '+' polarity of the ITO electrode for the light intensity of 10^{15} phot/(cm^2·s) and (a) 480 nm or (b) 720 nm wavelength, measured in the vacuum of $5·10^{-7}$ torr, for the sample with a 100 nm thick Ag electrode. The lighter curves stand for increasing voltage, the darker ones – for decreasing it; the EQE values are plotted with a negative sign, which indicates the electron flow direction towards the top Ag electrode.

Finally, the current–voltage characteristics changed less after the exposure to the air for the 100 nm–thick-Ag-electrode cell. It should be noted that the two regions observed on these plots for the 50 nm–thick-Ag-electrode cell are not present for the 100 nm–thick-Ag-electrode cell anymore: no long-tail region as in Fig. 4 is visible in Fig. 9. Only some decrease in the EQE values and the appearance a noticeable hysteresis are present, which indicates that even the protection offered by the 100 nm thick Ag layer is not enough to ensure the cell stability over a period of 180 minutes in the ambient air.

4. CONCLUSIONS

For inverted planar mixed halide perovskite $CH_3NH_3PbI_{3-x}Cl_x$ solar cells, the fill factor was found to increase when increasing the energy of the excitation photons: from 0.55 at 760 nm up to 0.82 at 400 nm for a freshly prepared cell with a 50 nm thick top Ag electrode, which had very high shunt resistance R_{shunt} of $3·10^7$ Ω·cm^2. Such high resistances indicate the low content of pinholes; in such a case the FF is mainly established by the recombination processes of the photogenerated charge carriers in the cell. This increase could be caused by hot polaron formation; the higher polaron energy, the lower their recombination. Also, other hypothetical explanations cannot be excluded. Thus, spectral dependences for the FF and the V_{OC} can provide an additional insight into the photovoltaic processes in the cell.

The kinetics of initial evolution of short-circuit photocurrent (SCP) EQE when vacuum was changed slowly from 5.10^{-7}torr to ambient atmosphere and pumped back to high vacuum was investigated. When initially vacuum diminished to ~ 10^{-4} torr even some increase of EQE was observed for cell with thin Ag electrode. This could be caused by incoming water molecules passivating surface trap states and/or improving intergrain contacts. By further decrease of vacuum some long period oscilations of SCP EQE were observed due to intricate diffusion processes of H_2O and O_2 until~$2·10^{-1}$ torr was reached. Letting the ambient air into the measurement chamber

caused a steep fall in EQE, but after the vacuum pumping was restarted, nearly initial values of the SCP EQE were observed again. Hence, this change for SCP EQE spectral dependence is reversible. However, spectral dependences for FF and V_{OC} bore strong evidence of irreversible degradation where FF diminished to less than 0.3 in the whole investigated spectrum, but V_{OC} dependence tail part increased up to 1.3 V at 420 nm. Thus, we can conclude that to get more full information about degradation processes in the cell we ought to investigate also spectral dependences for FF and V_{OC}, not only for SCP EQE

It was observed that the speed and the paths of degradation after the air inlet into the measurement chamber were strongly dependent on the thickness of the top Ag electrode. It means that for a 50 nm thick top electrode, exposure of the cell to the ambient air for 85 minutes and subsequent pumping back to $5 \cdot 10^{-7}$ torr induced dramatic changes in the shape of the current–voltage characteristics and thus in the V_{OC} and the FF. On the other hand, for the cell with a 100 nm thick top electrode, exposure to the ambient air for twice as longer period of 180 minutes and following pumping back led only to a moderate fall in the FF, whereas the shape of the current–voltage characteristics changed considerably less. Therefore, top Ag electrode thickness of at least 100 nm is recommended to increase the lifetime of the cells before their encapsulation.

ACKNOWLEDGEMENTS

REFERENCES

1. Kaulachs, I., Ivanova, A., Holsts, M., Roze, A., Flerov, A., Tokmakov, A., Mihailovs, I., & Rutkis, M. (2020). Perovskite $CH_3NH_3PbI_{3-x}Cl_x$ Solar Cells And Their Degradation (Part 1: A Short Review). *Latv. J. Phys. Tech. Sci. 2021, 1*, 44 -52. DOI: 10.2478/lpts-2021-0005.

2. Ivanova, A., Tokmakov, A., Lebedeva, K. Roze, M., & Kaulachs, I. (2017). Influence of the Preparation Method on Planar Perovskite $CH_3NH_3PbI_{3-x}Cl_x$ Solar Cell Performance and Hysteresis. *Latv. J. Phys. Tech. Sci.*, *54*, 58–68. DOI: 10.1515/lpts-2017-0027.

3. Xiao, Z., Bi, C., Shao, Y., Dong, Q., Wang, Q., Yuan, Y., … & Huang, J. (2014). Efficient, High Yield Perovskite Photovoltaic Devices Grown by Interdiffusion of Solution-Processed Precursor Stacking Layers. *Energy Environ. Sci., 7*, 2619–2623. DOI: 10.1039/C4EE01138D.

4. Seo, Y.-H., Kim, E.-C., Cho, S.-P., Kim, S.-S., & Na, S.-I. (2017). High-Performance Planar Perovskite Solar Cells: Influence of Solvent upon Performance. *Appl. Mater. Today*, *9*, 598–604. DOI: 10.1016/j.apmt.2017.11.003.

5. Shao, Y., Xiao, Z., Bi, C., Yuan, Y., & Huang, J. (2014). Origin and Elimination of Photocurrent Hysteresis by Fullerene Passivation in $CH_3NH_3PbI_3$ Planar Heterojunction Solar Cells. *Nat. Commun., 5*, 5784. DOI: 10.1038/ncomms6784.

6. Lopez-Varo, P., Jiménez-Tejada, J.A., García-Rosell, M., Ravishankar, S., Garcia-Belmonte, G., Bisquert, J., & Almora, O. (2018). Device Physics of Hybrid Perovskite Solar cells: Theory and Experiment. *Adv. Energy Mater.*, *8*, 1702772. DOI: 10.1002/aenm.201702772.

7. Wang, Q., Shao, Y., Dong, Q., Xiao, Z., Yuan, Y., & Huang, J. (2014). Large Fill-Factor Bilayer Iodine Perovskite Solar Cells Fabricated by a Low-Temperature Solution-Process. *Energy Environ. Sci., 7*, 2359–2365. DOI: 10.1039/C4EE00233D.

8. Kaulachs, I., Muzikante, I., Gerca, L., Shlihta, G., Shipkovs, P., Grehovs, V., … & Ivanova, A. (2012). Electrodes for GaOHPc:PCBM/P3HT:PCBM Bulk Heterojunction Solar Cell. *Chem. Phys., 405*, 46–51. DOI: 10.1016/j.chemphys.2012.06.007.

9. Kaulachs, I., & Silinsh, E. (1994). Molecular Triplet Exciton Generation via Optical Charge Transfer States in A-Metalfree Phthalocyanine, Studied by Magnetic Field Effects. *Latv. J. Phys. Tech. Sci.*, *5*, 12–22.

10. Shahbazi, M., & Wang, H. (2016). Progress in Research on the Stability of Organometal Perovskite Solar Cells, *Sol. Energy.*, *123*, 74–87. DOI: 10.1016/j.solener.2015.11.008.

11. Song, Z., Abate, A., Watthage, S.C., Liyanage, G.K., Phillips, A.B., Steiner, U., … & Heben, M.J. (2016). Perovskite Solar Cell Stability in Humid Air: Partially Reversible Phase Transitions in the PbI_2-CH_3NH_3I-H_2O System. *Adv. Energy Mater.*, *6*, 1600846. DOI: 10.1002/aenm.201600846.

12. Wang, Q., Chen, B., Liu, Y., Deng, Y., Bai, Y., Dong, Q., & Huang, J. (2017). Scaling Behavior of Moisture-Induced Grain Degradation in Polycrystalline Hybrid Perovskite Thin Films. *Energy Environ. Sci.*, *10*, 516–522. DOI: 10.1039/C6EE02941H.

13. Wang, D., Wright, M., Elumalai, N.K., & Uddin, A. (2016). Stability of Perovskite Solar Cells. *Sol. Energy Mater. Sol. Cells*, *147*, 255–275. DOI: 10.1016/j.solmat.2015.12.025.

14. Zhou, W., Zhao, Y., Shi, C., Huang, H., Wei, J., Fu, R., ... & Zhao, Q. (2016). Reversible Healing Effect of Water Molecules on Fully Crystallized Metal–Halide Perovskite Film. *J. Phys. Chem. C.*, *120*, 4759–4765. DOI: 10.1021/acs.jpcc.5b11465.

15. Eperon, G.E., Habisreutinger, S.N., Leijtens, T., Bruijnaers, B.J., van Franeker, J.J., DeQuilettes, D.W., … & Snaith, H.J. (2015). The Importance of Moisture in Hybrid Lead Halide Perovskite Thin Film Fabrication. *ACS Nano.*, *9*, 9380–9393. DOI: 10.1021/acsnano.5b03626.

16. Zhao, D., Sexton, M., Park, H.-Y., Baure, G., Nino, J.C., & So, F. (2015). High-Efficiency Solution-Processed Planar Perovskite Solar Cells with a Polymer Hole Transport Layer. *Adv. Energy Mater.*, *5*, 1401855. DOI: 10.1002/aenm.201401855.

17. Shi, Z., & Jayatissa, A. (2018). Perovskites-Based Solar Cells: A Review of Recent Progress, Materials and Processing Methods. *Materials (Basel)*, *11*, 729. DOI: 10.3390/ma11050729.

18. Wang, Q., Shao, Y., Xie, H., Lyu, L., Liu, X., Gao, Y., & Huang, J. (2014). Qualifying Composition Dependent p and n Self-Doping in CH3NH3PbI3. *Appl. Phys. Lett.*, *105*, 163508. DOI: 10.1063/1.4899051.

19. Chen, Q., Zhou, H., Song, T.-B., Luo, S., Hong, Z., Duan, H.-S., … & Yang, Y. (2014). Controllable Self-Induced Passivation of Hybrid Lead Iodide Perovskites toward High Performance Solar Cells. *Nano Lett.*, *14*, 4158–4163. DOI: 10.1021/nl501838y.

20. Yang, Y., Ostrowski, D.P., France, R.M., Zhu, K., van de Lagemaat, J., Luther, J.M., & Beard, M.C. (2016). Observation of a Hot-Phonon Bottleneck in Lead-Iodide Perovskites. *Nat. Photonics*, *10*, 53–59. DOI: 10.1038/nphoton.2015.213.

21. Niesner, D., Zhu, H., Miyata, K., Joshi, P.P., Evans, T.J.S., Kudisch, B.J., … & Zhu, X.-Y. (2016). Persistent Energetic Electrons in Methylammonium Lead Iodide Perovskite Thin Films. *J. Am. Chem. Soc.*, *138*, 15717–15726. DOI: 10.1021/jacs.6b08880.

22. Yang, J., Wen, X., Xia, H., Sheng, R., Ma, Q., Kim, J., … & Conibeer, G. (2017). Acoustic-Optical Phonon Up-Conversion and Hot-Phonon Bottleneck in Lead-Halide Perovskites. *Nat. Commun.*, *8*, 14120. DOI: 10.1038/ncomms14120.

23. Zhu, H., Miyata, K., Fu, Y., Wang, J., Joshi, P.P., Niesner, D., ... & Zhu, X.-Y. (2016). Screening in Crystalline Liquids Protects Energetic Carriers in Hybrid Perovskites. *Science*, *353*, 1409–1413. DOI: 10.1126/science.aaf9570.

24. Bretschneider, S.A., Laquai, F., & Bonn, M. (2017). Trap-Free Hot Carrier Relaxation in Lead–Halide Perovskite Films. *J. Phys. Chem. C.*, *121*, 11201–11206. DOI: 10.1021/acs.jpcc.7b03992.

25. Guo, Z., Wan, Y., Yang, M., Snaider, J., Zhu, K., & Huang, L. (2017). Long-Range Hot-Carrier Transport in Hybrid Perovskites Visualized by Ultrafast Microscopy. *Science*, *356*, 59–62. DOI: 10.1126/science.aam7744.

26. Frost, J.M., Whalley, L.D., & Walsh, A. (2017). Slow Cooling of Hot Polarons in Halide Perovskite Solar Cells. *ACS Energy Lett.*, *2*, 2647–2652. DOI: 10.1021/acsenergylett.7b00862.